

# Design, Control, and Experimentation of Internally-Actuated Rovers for the Exploration of Low-gravity Planetary Bodies

• • • • •

**Benjamin J. Hockman**

*Department of Mechanical Engineering, Stanford University, Stanford, California 94305*  
*e-mail: bhockman@stanford.edu*

**Andreas Frick, Robert G. Reid, and Issa A.D. Nesnas**

*Jet Propulsion Laboratory, California Institute of Technology, Pasadena, California 91109*  
*e-mail: andreas.frick@jpl.nasa.gov, robert.g.reid@jpl.nasa.gov, issa.a.nesnas@jpl.nasa.gov*

**Marco Pavone\***

*Department of Aeronautics and Astronautics, Stanford University, Stanford, California 94305*  
*e-mail: pavone@stanford.edu*

Received 21 November 2015; accepted 4 April 2016

This paper discusses the design, control, and experimentation of internally-actuated rovers for the exploration of low-gravity (micro-g to milli-g) planetary bodies, such as asteroids, comets, or small moons. The rover is actuated by spinning three *internal* flywheels, which allows all subsystems to be packaged in one sealed enclosure and enables the platform to be minimalistic, thereby reducing its cost. By controlling the spin rate of the flywheels, the rover can achieve large surface coverage by attitude-controlled hops, fine mobility by tumbling, and coarse instrument pointing by changing the orientation relative to the ground. We first discuss the dynamics of such rovers, their control, and key design features (e.g., flywheel shape and orientation, geometry of external spikes, and system engineering aspects). We then discuss the design and control of a first-of-a-kind test bed that enables the accurate emulation of a microgravity environment for mobility experiments, which consists of a three-degree-of-freedom gimbal attached to an actively controlled gantry crane. Finally, we present experimental results on the test bed that provide key insights for rover control and validate our theoretical analysis. © 2016 Wiley Periodicals, Inc.

## 1. INTRODUCTION

The exploration of small bodies in the Solar System, such as comets, asteroids, or irregular moons, has become a central objective for planetary exploration (Castillo Rogez, Pavone, Nesnas, Hoffman, et al., 2012; NRC, 2011). In fact, recent ground- and space-based observations indicate that the exploration of small bodies would collectively address all three of the following main science objectives prioritized by NASA's recent decadal survey: (i) the characterization of the early history of the Solar System, (ii) the search for planetary habitats, and (iii) an improved understanding about the nature of planetary processes (NRC, 2011). While measurements of some chemical and physical properties

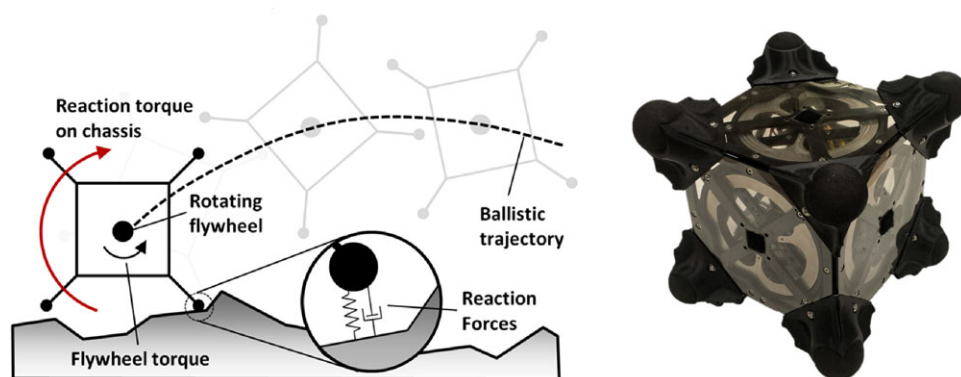
can be obtained by remote sensing from space telescopes or orbiters, measurements that constrain composition (e.g., origin science) and measurements of physical properties that fill strategic knowledge gaps for human exploration require direct contact with the surface at multiple locations for extended time periods (Castillo Rogez, Pavone, Nesnas, Hoffman, et al., 2012). Accordingly, *controlled* mobility in low-gravity environments (micro-g to milli-g) has been identified by the National Research Council in 2012 as one of NASA's high priorities for technology development (NRC, 2012).

Microgravity mobility is challenging due to the virtual absence of traction. A number of approaches to mobility have been proposed in the past two decades, which can be roughly divided into four classes: mobility via thrusters, wheels, legs, and hopping. Thrusters have a number of disadvantages for mobility, including mechanical and operational complexity, limited lifetime (due to propellant limitation), and potential for surface contamination. Wheeled vehicles rely on surface normal forces to create

\*Project principal investigator.

A preliminary version of this paper has appeared at the 2015 Conference on Field and Service Robotics (Hockman, Frick, Nesnas, & PavoneHockman et al., 2015).

Direct correspondence to: Marco Pavone, e-mail: pavone@stanford.edu



**Figure 1.** Left: by rotating internal flywheels, surface reaction forces make the rover tumble/hop. Right: our current prototype without avionics, covers, or solar panels. The cubic structure encloses three flywheels and is protected by external spikes on each of its corners.

lateral traction—a force that is orders of magnitude weaker in microgravity environments. As a result, wheeled systems are bound to extremely low speeds [1.5 mm/s per previous JPL studies (Jones, 2000)] and can easily lose contact with the surface when traversing rocky terrain, resulting in uncontrollable tumbling. Legged systems rely on anchoring devices at the tips, which are mechanically complex and highly dependent on (largely unknown) surface properties. The challenge of anchoring on a small body has been well illustrated by the recent Philae’s landing and failed anchoring on the surface of a comet (Glassmeier, Boehnhardt, Koschny, Kührt, & Richter, 2007; Hand, 2014). Alternatively, *hopping* systems use the low-gravity environment to their advantage. Space agencies such as NASA (Fiorini & Burdick, 2003; Jones, 2000), RKA (Sagdeev & Zakharov, 1989), ESA (Dietze et al., 2010), and JAXA (JAXA, 2011) have all recognized this advantage and have designed a number of hopping rovers. However, existing platforms do not appear to allow precise traverses to designated targets in low-gravity environments, as required for targeted *in situ* sampling.

**Statement of Contributions:** In this paper, we present and discuss our ongoing efforts toward the design of a microgravity rover aimed at controlled mobility. The platform uses internal actuation (three mutually orthogonal flywheels) to generate reaction torques, enabling directional hopping capabilities. Specifically, by applying a controlled *internal* torque between the flywheels and the platform, one generates an angular rotation of the platform. In turn, this angular rotation gives rise to surface reaction forces at external contact points, which lead to either tumbling (i.e., pivoting around a spike tip) or hopping (when the reaction forces are large enough), as shown in Figure 1, left. External spikes protect the platform during ground collisions and provide the primary contact interface with the surface (see Figure 1, right). With this design, all subsystems are packaged in one sealed enclosure, which enables the rover to

be minimalistic and drastically reduces its cost. Henceforth, we will refer to such a rover as a “hopper,” inspired by its primary mode of mobility.

This paper builds upon a number of previous results on microgravity internal actuation, namely JAXA (2011), which first proposed the use of internal actuation (specifically a single flywheel mounted on a turntable for limited motion control), and Allen et al. (2013) and Reid, Roveda, Nesnas, Pavone et al. (2014), which consider a torque-controlled three-flywheel configuration and present experimental results on three degree-of-freedom (DoF) test beds. This paper is also related to Gajamohan, Merz, Thommen, & D’Andrea (2012), which considers the problem of balancing a cubic body on a corner by actuating three orthogonal flywheels, and to Romanishin, Gilpin, & Rus (2013), which uses a single gimbaled flywheel within small cubes for studying reconfigurable lattice structures.

Specifically, the contributions of this paper are three-fold. First, we characterize the dynamics of the hopper and develop hybrid control algorithms for precise mobility (Section 2). Our approach leverages a conservation of angular momentum argument, as opposed to the energy approach in Allen et al. (2013) used to characterize hopping maneuvers. Second, in Section 3 we discuss the hopper design with special attention to key mobility components, and we present a preliminary system architecture design for a reference mission to Phobos. Third, we present a first-of-a-kind 6 DoF microgravity test bed in Section 4 designed specifically for this class of hoppers, and we discuss its capabilities and limitations. The test bed consists of a 3 DoF gimbal attached to an actively controlled gantry crane, and it represents, on its own, a major step toward characterizing and validating microgravity mobility [previous test beds only allowed 3DoF tests, e.g., the Atwood machine (Reid, Roveda, Nesnas, Pavone et al., 2014), or tests of the first phases of motion, e.g., parabolic flights and drop towers (Yoshimitsu, Kubota, Nakatani, Adachi, & Saito, 1999)].

**Table I.** Motion primitives classified by the magnitude and direction of the angular velocity.

		Direction with respect to surface		
		Parallel	Angled	Normal
Magnitude	Low	Tumble	Twisting tumble	Twist
	High	Hop	Twisting hop	Tornado

Finally, the test bed is utilized to conduct several mobility experiments in Section 5 as a means of validating and refining the dynamics and control insights derived in Section 2.

A preliminary version of this paper appeared as Hockman, Frick, Nesnas, & Pavone (2015). This extended and revised version contains a number of additional contributions: (i) The dynamics and control analysis has been extended to consider the full range of motion primitives (see Table I), including oblique hops and twisting maneuvers. (ii) The discussion of the test bed in Section 4 now offers a more comprehensive survey of design insights and performance analysis, highlighting its benefits and limitations. (iii) Finally, several additional experiments have been conducted in the test bed to study a much wider spectrum of motion primitives.

## 2. DYNAMICS AND CONTROL

When in free flight, the hopper simply behaves like an attitude-controlled spacecraft, for which the dynamics are well-known. A number of interesting behaviors arise, however, when the hopper actuates its flywheels *while in contact with the surface* of a small body. In general, the three orthogonal flywheels allow for any arbitrary torque to be applied to the hopper—large abrupt torques via mechanical brakes and smaller, more controlled torques via motors. It is convenient to *classify* the rather large space of possible maneuvers into a set of *motion primitives*.

Table I proposes a classification of motion primitives based on the magnitude and direction of the hopper’s angular velocity. Focusing on motion primitives allows for closed-form insights to be derived from simplified analytical models. In particular, three of the six motion primitives are especially useful for mobility:

- **Hopping** occurs when sufficient force is generated against the surface to launch the hopper forward in a ballistic trajectory, anywhere from one body-length to hundreds of meters. Thus, it is the primary mode of mobility for large distance coverage.
- **Tumbling** is simply a less energetic form of hopping, whereby the hopper rotates about a pair of spikes without losing ground contact. Tumbling is less likely to induce random bouncing, and thus offers a much more precise, albeit slower, form of mobility.

- **Twisting** is not a direct form of mobility, but rather a way of changing orientation by turning in place. Such a maneuver can help to point instruments or enable subsequent hops/tumbles from a different orientation.

Hopping and tumbling about axes parallel to the surface is more controllable than twisting hops/tumbles about arbitrary inclined axes (as we will discuss in Section 2.1.2), and they are more amenable to an analytical treatment. A “Tornado” maneuver (inspired by the way in which it flings nearby surface regolith) is an energetic twist that typically also hops up due to surface imperfections—not a particularly controllable motion, but potentially useful for escaping from being stuck or buried. In this section, we study the dynamics and control of these three primary motion primitives, establishing a suite of *controllable* maneuvers whose concatenation can provide targeted mobility.

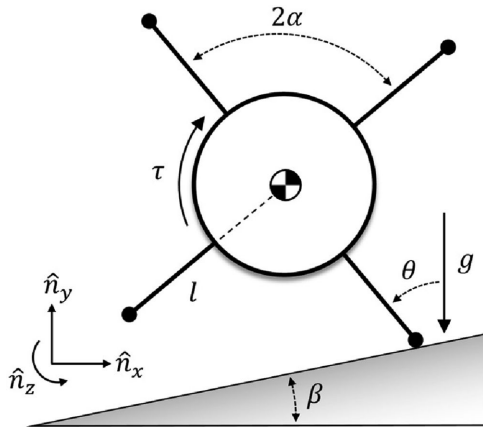
Our analysis extends earlier studies for this class of hoppers [chiefly Allen et al. (2013) and Reid, Roveda, Nesnas, Pavone et al. (2014)] along a number of dimensions. First, our analysis of hopping and tumbling maneuvers is based on a conservation of angular momentum argument, which directly accounts for energy losses. In contrast, Allen et al. (2013) and Reid, Roveda, Nesnas, Pavone et al. (2014) mostly rely on an energy-conservation approach, which, as we will show in Section 2.2, can lead to gross underestimates in required flywheel actuation. Second, we study the effect of an inclined surface. Third, we study the dynamics and control of a twisting maneuver. Fourth, we extend the two-dimensional (2D) hopping analysis to configurations in which the hopper pivots about a single spike for directional control. Fifth, and perhaps most importantly, we study in detail control strategies for these motion primitives.

### 2.1. Hopping Dynamics and Control

As the primary mode of mobility, understanding the fundamental dynamics that govern *hopping* trajectories is a critical step toward characterizing the hopper’s mobility capabilities. In this section, we consider two analytical models to derive useful control laws: (i) the first examines a simplified 2D model for the case of single-axis hops, and (ii) a more general 3D model of the hopper that pivots about only one of its spikes.

#### 2.1.1. Single-axis Hopping

In the case of hopping and tumbling about a single axis (i.e., with just one flywheel), the hopper pivots about a *pair* of spikes, allowing for a *planar* (2D) representation of the dynamics. The hopper is modeled as a disk with equispaced rigid spikes attached to it, similar to the model commonly used in the field of passive dynamic walking (McGeer, 1990). At the center of mass, a motor drives a single flywheel, producing a torque on the hopper (see Figure 2). This model can



	Definition
$\theta$	hopper's angle
$\beta$	surface inclination
$l$	spikes' length from CG
$m_p$	total mass of hopper
$I_f$	flywheel's rotational inertia
$I_p$	hopper's rotational inertia
$\tau$	flywheel's torque on hopper
$2\alpha$	angle in between spikes
$\omega_f$	flywheel angular velocity in $\hat{n}_z$
$g$	gravity acceleration

**Figure 2.** 2D model: A hopper is modeled as a rigid body that pivots on an inclined surface. This planar representation is also the basis for the tumbling analysis in Section 2.2.

be thought of as a 2D vertical slice of the hopper, orthogonal to the applied torque.

The key assumption in our study is that the stance spike acts as a pin joint and does not slip. Under this assumption, the 2D model of the hopper is uniquely described by two states,  $\theta$  and  $\dot{\theta}$ . See Figure 2 for a detailed description of all parameters. A detailed study of the transition between pivoting and sliding motion of the spike tip can be found in Reid, Roveda, Nesnas, Pavone et al. (2014) for a Coulomb friction model. One can show that the no-slip assumption is a reasonable approximation for coarse spike geometries where  $(\theta - \beta) > \tan^{-1}(1/\mu_d)$ , where  $\mu_d$  is the coefficient of dynamic friction. For the rubber spike tips on our current prototype,  $1 < \mu_d < 1.5$ , which, as validated via simulations in Section 2.1.1 and experiments in Section 5.1, is high enough to justify this no-slip assumption. This assumption, however, would not hold in cases in which the hopper operates on nonrigid surfaces (i.e., loose regolith), whereby the slip properties are governed by frictional interactions with granular media. This aspect is left for future research.

A hopping maneuver consists of a stride phase when the system is supported by a single stance spike (in the 2D world), and a flight phase when the stance spike leaves the ground. We study the flywheel's torque needed to cause the hopper to hop to the right at a desired speed  $v_h$  and angle  $\theta_h$  (the subscript "h" denotes quantities evaluated at the hopping instant). Assume that the hopper starts at rest on the inclined surface and applies a sufficient torque  $\tau(t)$  to induce a clockwise rotation about its stance spike. For the stride phase (i.e., before ground contact is lost), the equation of motion is that of an inverted pendulum and can be easily written as

$$\ddot{\theta}(t) = \frac{m_p g l \sin \theta(t) - \tau(t)}{I_p + m_p l^2}, \quad (1)$$

as also derived in Allen et al. (2013). The first thing to note is that there exists a minimum torque that will cause the hopper to initiate a clockwise rotation (i.e.,  $\ddot{\theta} < 0$ ) from rest:

$$\tau_{\min} = m_p g l \sin(\alpha + \beta). \quad (2)$$

For typical gravity levels of interest (10–1,000  $\mu g$ ), small motors of only a few Watts would be sufficient to exceed this torque. Secondly, by studying the free body diagram of the system, one can readily show that in order to obtain a negative normal force (i.e., loss of ground contact), it is required that

$$|\dot{\theta}(t_h)| > \sqrt{\frac{m_p g \cos \beta + \frac{\tau(t_h)}{l} \sin(\theta(t_h) - \beta)}{m_p l \cos[\theta(t_h) - \beta]}}. \quad (3)$$

For a level terrain (i.e.,  $\beta \approx 0$ ) and with no input torque,  $|\dot{\theta}(t_h)|_{\min} = \sqrt{g/[l \cos \theta(t_h)]}$ , which corresponds to a *minimum hop distance* on the order of  $2l$ .

In this section, we study a control strategy that leverages (2) by slowly spinning up the flywheels with motor torque  $\tau < \tau_{\min}$ , such that the hopper remains grounded. When the desired flywheel speed is achieved, a high-torque mechanical brake (discussed in Section 3.1) is applied and a hop is initiated. This approach is attractive as it is simple, it does not cause momentum buildup in the flywheels, and it rapidly transfers energy for more aggressive hops. Therefore, a control strategy of particular interest assumes "instantaneous" momentum transfer from the flywheel to the hopper.<sup>1</sup>

By equating the initial angular momentum of the flywheel ( $I_f \omega_f$ ) to the resulting angular momentum of the hopper about the spike tip [ $\dot{\theta}(I_p + m_p l^2)$ ], and assuming that a hop is initiated immediately after momentum transfer [i.e.,

<sup>1</sup>The experimental results in Section 3.1 validate this assumption.



$v_h = l\dot{\theta}(0^+)$ , the resulting hop velocity, angle, and lateral distance are given, respectively, by

$$v_h = l\omega_f \left( \frac{I_f}{I_p + m_p l^2} \right), \quad \theta_h = \alpha + \beta, \quad d_h = \frac{v_h^2}{g} \sin(2\theta_h). \quad (4)$$

A few interesting observations can be made from these results. First, in this regime, the hop angle is governed exclusively by the spike geometry and surface inclination. To maximize the lateral distance of the parabolic trajectory [which scales as  $\sin(2\theta_h)$ ], a  $45^\circ$  hop is desired. This is one of the reasons why our current design has a cubic spike geometry (i.e.,  $\alpha = 45^\circ$ ); see Section 3. Second, we define the energy transfer efficiency as

$$\eta := \frac{E(t^+)}{E(t^-)} = \frac{I_f}{I_p + m_p l^2}, \quad (5)$$

where  $E(t^-)$  is the energy of the system just before actuation (flywheel kinetic energy), and  $E(t^+)$  is the energy just after actuation (hopper's kinetic energy). Interestingly, the efficiency is given by the ratio of flywheel inertia to hopper's inertia *about the spike tip*, which depends quadratically on the length of the spikes. Hence, there is an important tradeoff between the capability of negotiating obstacles (that would require long spikes) and the actuation efficiency (that prefers short spikes). For our current prototype (augmented with dead mass as a stand-in for scientific payload),  $\eta \approx 0.01$ . This result is critically enabled by angular momentum arguments.

Now, Eqs. (4) and (5) can be combined to develop an expression for the flywheel speed ( $\omega_f$ ) required to cover a lateral distance  $d_h$ :

$$\omega_f(d_h) = \sqrt{\frac{d_h g}{\eta^2 l^2 \sin[2(\alpha + \beta)]}}. \quad (6)$$

For a square geometry this expression is minimized for flat terrain, but it tends toward infinity as  $\beta \rightarrow 45^\circ$ . This motivates the potential utility of controllable friction brakes, which can extend the duration of the stride phase and thus control the hop angle.

In the more general case when momentum transfer is *not* assumed to be instantaneous, one can regard the initial flywheel speed ( $\omega_f$ ) and constant braking torque ( $\bar{\tau}$ ) as the *two* control variables. In bringing the flywheel to a full stop, the control variables are related by  $\bar{\tau} \Delta t = I_f \omega_f$ , where  $\Delta t$  is the time duration of braking. In the limit as  $\Delta t \rightarrow 0$ , the impulsive torque corresponds to the case of instantaneous momentum transfer. To study the case when  $\Delta t$  is finite, the nonlinear differential equations of motion given by Eq. (1) must be solved numerically. However, for aggressive hops, one can assume that  $\bar{\tau} \gg m_p g l \sin(\theta)$ , so Eq. (1) can be well approximated by the linear second-order ordinary

differential equation,  $\ddot{\theta}(t) \approx -\bar{\tau}/(I_p + m_p l^2)$ . For high enough torques, the hop criterion in (3) is not met until immediately after actuation (i.e., at  $t_h = \Delta t = \omega_f I_f / \bar{\tau}$ ), so the hop velocity, angle, and resulting distance can be determined by integration:

$$v_h = l\eta\omega_f, \quad \theta_h = \alpha - \frac{\eta I_f \omega_f^2}{2\bar{\tau}}, \quad d_h = \frac{v_h^2 \sin(2\alpha - \eta I_f \omega_f^2 / \bar{\tau})}{g}. \quad (7)$$

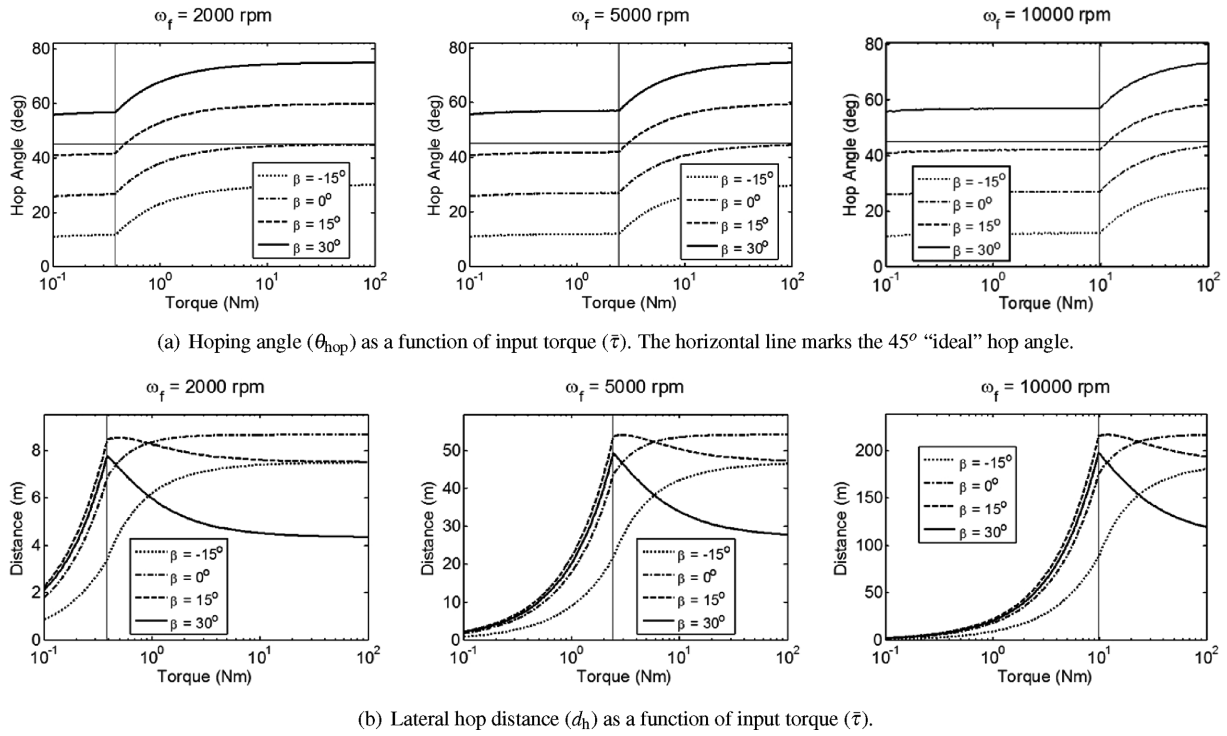
Solving for the control inputs,  $\bar{\tau}$  and  $\omega_f$ , now requires solving this set of nonlinear algebraic equations. To better visualize these results and to validate the pivoting assumptions, numerical simulations were generated based on a full 6 DoF model, including normal spring/damper and tangential Coulomb friction contact forces [as used in Reid, Roveda, Nesnas, Pavone et al. (2014)].

The plots in Figure 3 illustrate the hopping angle and distance that result from a constant braking torque,  $\bar{\tau}$ . Each plot represents a different flywheel speed (2,000, 5,000, and 10,000 rpm). The kink in each curve marks the threshold of an “early hop”—the torque level ( $\bar{\tau}_s$ ) below which surface contact is lost before the flywheel is fully stopped. In other words, for a given flywheel speed,  $\bar{\tau}_s$  is the minimum braking torque that should be applied to convert all of the flywheel's available kinetic energy to forward motion. This threshold (marked by a vertical line) is in very close agreement with predictions based on (3).

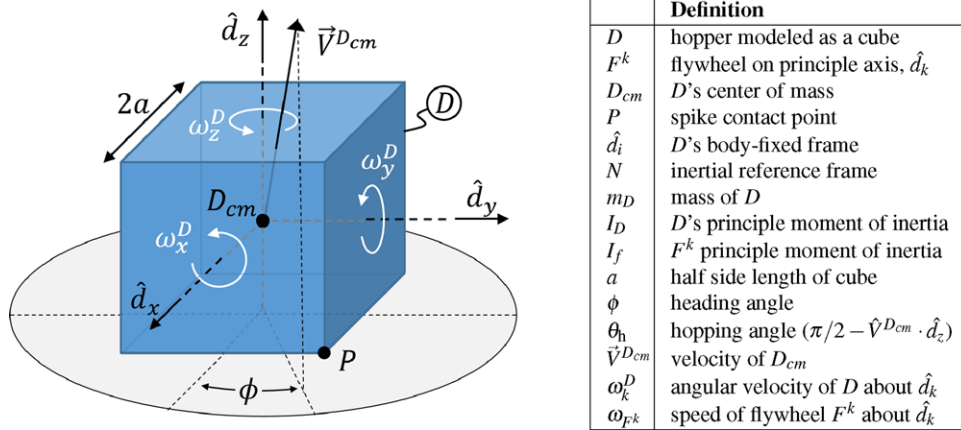
Figure 3(b) shows that for  $\beta \leq 0$  (i.e., hopping downhill), travel distance increases as the torque is increased. However, the situation is different when considering inclined poses ( $\beta \geq 0$ ), whereby high torque inputs result in high-angle arching hops—an undesirable effect for distance coverage but potentially useful for getting out of pits. The peaks in these distance curves are in agreement with (6).

## 2.1.2. Hopping Directional Control

The analytical model presented in Section 2.1.1 is well suited for *single-axis* hops because the out-of-plane degree of freedom is locked by having two spikes in contact with the surface. For a cubic design, this only allows for hops in  $90^\circ$  directional increments, analogous to a “Manhattan-style” mobility approach. There are two ways in which a finer resolution of directional control can be achieved: (i) using a twist maneuver as discussed in Section 2.3 to point a primary axis toward the desired heading and execute a single-axis hop, or (ii) hopping directly over a single spike about an “oblique” axis. The latter approach is faster, as it avoids an intermediate twist maneuver and may also be useful in situations in which an accurate twist maneuver is difficult due to terrain roughness. In this section, we will consider a 3D model of the hopper to study the dynamics and control of such oblique hops (see Figure 4).



**Figure 3.** Resulting hop angles and distances as functions of input torque for three initial flywheel speeds:  $\omega_f = 2,000, 5,000$ , and  $10,000$  rpm (the  $x$  axis is in logarithmic scale). Each curve corresponds to a particular surface inclination  $\beta$ . The vertical line on each graph marks the minimum torque at which the flywheel can be fully stopped before a hop is initiated [see Eq. (3)]. Results are based on Phobos’ gravity level ( $0.0058 \text{ m/s}^2$ ) and parameters of our prototype (see Section 3.1).



**Figure 4.** 3D model: A hopper is modeled as a uniform cube that pivots about a corner.

In general, when pivoting about a single spike, the hopper behaves like a ball-jointed inverted pendulum with three degrees of freedom and complicated nonlinear dynamics. However, just as in Section 2.1.1, the assumption of

instantaneous momentum transfer (i.e., high friction brakes) can again be leveraged to collapse the dynamics of interest to an instant in time. In this way, conservation of angular momentum can again be invoked (this time about the single

spike contact) to relate the hopper's rotation rate ( ${}^N\vec{\omega}^D$ ) immediately after braking, to the initial flywheel speeds ( $\omega_{F^k}$ ):

$$\left( \sum_{k=x,y,z} {}^N\vec{H}^{F^k/P} \right) \Big|_{t=0^-} = \left( {}^N\vec{H}^{D/P} \right) \Big|_{t=0^+} = \left( \vec{I}^{D/D_{CM}} + m_D [(\vec{r}^{P/D_{CM}} \cdot \vec{r}^{P/D_{CM}})\mathbf{I} - (\vec{r}^{P/D_{CM}})(\vec{r}^{P/D_{CM}})^T] \right) \cdot {}^N\vec{\omega}^D \Big|_{t=0^+},$$

$$\begin{bmatrix} I_f & 0 & 0 \\ 0 & I_f & 0 \\ 0 & 0 & I_f \end{bmatrix} \begin{bmatrix} \omega_{F^x} \\ \omega_{F^y} \\ \omega_{F^z} \end{bmatrix} \Big|_{t=0^-} = \begin{bmatrix} I_D + 2m_D a^2 & -m_D a^2 & m_D a^2 \\ -m_D a^2 & I_D + 2m_D a^2 & m_D a^2 \\ m_D a^2 & m_D a^2 & I_D + 2m_D a^2 \end{bmatrix} \begin{bmatrix} \omega_x^D \\ \omega_y^D \\ \omega_z^D \end{bmatrix} \Big|_{t=0^+} \quad \text{for } \vec{r}^{P/D_{CM}} = [a \ a \ -a]^T. \quad (8)$$

This equation uses Steiner's theorem to express the inertia tensor of the hopper about the spike tip ( $P$ ), which produces non-negligible products of inertia. Here, the principal moments of inertia are assumed to be equal due to the symmetric geometry of the hopper. Refer to Figure 4 for definitions of all symbols.

When pivoting about point  $P$ , the hopper's velocity ( ${}^N\vec{V}^{D_{CM}}$ ) is constrained such that  $D_{CM}$  moves along the arc defined by  $\vec{r}^{D_{CM}/P}$ ; that is,  ${}^N\vec{V}^{D_{CM}} = {}^N\vec{\omega}^D \times \vec{r}^{D_{CM}/P}$ . Thus, given a desired heading angle ( $\phi$ ), the resulting hop angle ( $\theta_h$ ) is geometrically constrained to be

$$\theta_h = \tan^{-1}(\cos \phi + \sin \phi). \quad (9)$$

For  $\phi = 0^\circ$  (akin to a single-axis hop), this predicts a hop angle of  $\theta_h = 45^\circ$ , which indeed agrees with Eq. (4) for a cubic geometry. For hopping directly over a single spike (i.e.,  $\phi = 45^\circ$ ), Eq. (9) is maximized, predicting a hop angle of  $\theta_h = 54.7^\circ$ . Although not as efficient for long-distance hops, a steeper hop angle may be useful for ascending steep terrain or escaping from pits. Incidentally, the force vector imparted by the ground is exactly parallel to  ${}^N\vec{V}^{D_{CM}}$ , so hop angles ranging between  $45^\circ$  and  $55^\circ$  generate enough normal force to validate the no-slip assumption, as discussed for the 2D model in Section 2.1.1. Now, given a desired heading angle ( $\phi$ ), hop angle ( $\theta_h$ ), and speed ( $v_h$ ), the velocity vector is given by

$${}^N\vec{V}^{D_{CM}} = \frac{v_h}{\sqrt{2(1 + \sin \phi \cos \phi)}} \begin{bmatrix} \cos \phi \\ \sin \phi \\ \sin \phi + \cos \phi \end{bmatrix}. \quad (10)$$

So far, (8) relates  ${}^N\vec{\omega}^D$  to the control inputs ( $\omega_{F^k}$ ), and (10) relates  ${}^N\vec{V}^{D_{CM}}$  to the desired trajectory, governed by  $\phi$  and  $v_h$ . However, to formulate a control law relating flywheel inputs to a desired trajectory,  ${}^N\vec{\omega}^D$  must be calculated as a function of  ${}^N\vec{V}^{D_{CM}}$ , which is an ill-posed problem, in general. In other words,  ${}^N\vec{V}^{D_{CM}}$  does not uniquely define  ${}^N\vec{\omega}^D$ . Intuitively, it makes sense that the angular velocity component about  $\vec{r}^{D_{CM}/P}$  does not influence  ${}^N\vec{V}^{D_{CM}}$ . There are many ways to constrain  ${}^N\vec{\omega}^D$  such that it is uniquely defined by  ${}^N\vec{V}^{D_{CM}}$ . For the case of "pure" hopping (refer to

Table I), the angular velocity should be parallel to the surface,<sup>2</sup> which forces  $\omega_z^D = 0$ . Thus, for  $\vec{r}^{P/D_{CM}} = [a \ a \ -a]^T$  and  $\omega_z^D = 0$ , it follows that

$${}^N\vec{\omega}^D = \frac{v_h}{a\sqrt{2(1 + \sin \phi \cos \phi)}} \begin{bmatrix} -\sin \phi \\ \cos \phi \\ 0 \end{bmatrix}. \quad (11)$$

Finally, Eqs. (8) and (11) can be combined to calculate the control inputs,  $\omega_{F^k}$ . Interestingly, even though  $\omega_z^D = 0$ ,  $\omega_{F^z} \neq 0$  in general, which can be attributed to the effects of products of inertia in  $\vec{I}^{D/P}$ . Note that Eqs. (8)–(11) are derived for a particular spike contact point,  $P$ , although the same arguments can be used to derive similar expressions for any other spike. Furthermore, by constraining the hopper's rotation to be parallel with the surface, the heading angle is bounded to  $0 \leq \phi \leq \pi/2$  for pivoting about  $P$ . Equation (11) can be modified to perform twisting hops, which expand this range to as much as  $-\pi/4 \leq \phi \leq 3\pi/4$ . However, this also produces shallower hop angles, which may violate the no-slip contact assumption for low friction surfaces.

### 2.1.3. Travel Speed

The analysis of Section 2.1.1 can be extended to answer the question, "How fast can the hopper travel?" More specifically, the speed we care about is the *gross* speed at which the hopper can traverse a relatively flat and unobstructed terrain. The duration of a single hopping maneuver can be thought of as the sum of the time to spin up the flywheels ( $T_{\text{spin}}$ ) and the time of flight ( $T_{\text{flight}}$ ), where

$$T_{\text{spin}} = K_S \left( \frac{\sqrt{2}\omega_f I_f}{m_p g l} \right), \quad T_{\text{flight}} = K_B \left( \frac{\sqrt{2}\eta l \omega_f}{g} \right),$$

$$d_{\text{hop}} = K_D \left( \frac{(\eta l \omega_f)^2}{g} \right). \quad (12)$$

These equations result directly from Eqs. (1) and (4), and assuming  $\theta_{\text{hop}} = \alpha = 45^\circ$ . Here,  $K_S$  represents a safety

<sup>2</sup>Other types of constraints can be conceived for twisting hops, but care must be taken to ensure that they do not force neighboring spikes into the surface, which would violate the single-point pivoting assumption.

factor to prevent counter rotation during flywheel spin-up,  $K_B$  accounts for residual bouncing as a proportional correction factor on the flight time of the first parabola, and  $K_D$  is also a proportional correction factor on hop distance to account for bouncing as well as for deviations in heading. Based on observations from simulations, conservative estimates are  $K_B = 2$  and  $K_S, K_D = 1.2$ . Combining (12) and (6) yields the average expected speed:

$$\begin{aligned} \bar{v} &= \frac{d_{\text{hop}}}{T_{\text{flight}} + T_{\text{spin}}} = \frac{\sqrt{2d_h g}}{2} \left( \frac{K_D \eta m_p l^2}{K_B \eta m_p l^2 + K_S I_f} \right) \\ &\approx \frac{\sqrt{2d_h g}}{2} \left( \frac{K_D}{K_B + K_S} \right). \end{aligned} \quad (13)$$

The above approximation assumes  $I_p + m_p l^2 \approx m_p l^2$ , which is reasonable for our prototype ( $m_p l^2 = 0.065$  and  $I_p = 0.013$ ). Interestingly,  $\bar{v}$  depends on the square root of hop distance and gravity, indicating that farther hops result in faster net motion, and motion on bodies with weaker gravity is slower. On Phobos ( $g = 0.0058 \text{ m/s}^2$ ), with the parameters of our current prototype, the parameters  $K_S, K_B$ , and  $K_D$  defined above, and for an average 10 m hop, we can expect a net speed of about 7 cm/s. However, for longer excursions, hops of 100 m are reasonable (i.e.,  $\omega_f = 6,000 \text{ rpm}$ ), and net speed could increase to over 20 cm/s.

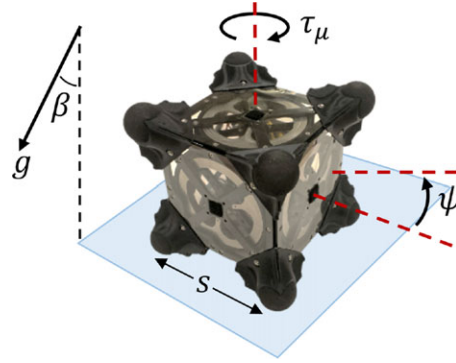
## 2.2. Tumbling Dynamics and Control

Tumbling refers to a rotational maneuver whereby the hopper pivots about one or two spikes and lands on an adjacent face without losing surface contact. Although tumbles about a single spike are possible, the dynamics of the hopper about a single point of contact have 3 DoF and are relatively uncontrollable compared to pivoting over a pair of spikes. Therefore, the analysis here will only consider single-axis tumbles, again using the 2D model presented in Figure 2. In this context, the goal of a tumbling maneuver is to pivot to the right and land on the next consecutive spike such that its orientation is incremented by  $-2\alpha$ .

To characterize actuation bounds for tumbling, the actuation is regarded as an instantaneous transfer of momentum, similar to the hopping analysis in Section 2.1.1. Accordingly, the initial kinetic energy of the hopper at  $t = 0^+$  can be equated to the gravitational potential energy at the tumbling apex ( $\theta = 0$ ). This yields an expression for the *minimum* flywheel velocity required to vault the hopper over its leading spike:

$$\omega_{f, \min} = \sqrt{\frac{2m_p g l [1 - \cos(\alpha + \beta)]}{\eta I_f}}. \quad (14)$$

Note that a similar result is provided in Allen et al. (2013), but it does not directly account for energy losses or accommodate inclined surfaces. This leads to an underestimate of



**Figure 5.** A twisting maneuver: the hopper turns in place to change orientation.

control input by a factor of  $1/\sqrt{\eta} \approx 10$ , thus illustrating the importance of an angular momentum approach.

To characterize the *maximum* flywheel velocity for tumbling, consider the hop criterion given by (3) and a zero torque input for  $t \geq 0^+$ . It follows that  $\theta(t)$  and  $|\dot{\theta}(t)|$  both decrease with time. Thus, if surface contact is lost, it will occur just after momentum transfer when  $\theta(0^+) = \alpha + \beta$ , and  $|\dot{\theta}(0^+)| = \eta \omega_f$ . This yields the maximum flywheel velocity to perform a tumble *without* hopping:

$$\omega_{f, \max} = \sqrt{\frac{g \cos \beta}{\eta^2 l \cos \alpha}}. \quad (15)$$

Interestingly, there exists an inclination angle,  $\beta_{\max}$ , for which  $\omega_{f, \min} = \omega_{f, \max}$  and tumbling is impossible. For a square geometry ( $\alpha = 45^\circ$ ),  $\beta_{\max} \approx 30^\circ$ . Also, as expected,  $\omega_{f, \min} = 0$  when  $\beta = -\alpha$ , which corresponds to the declination angle at which the hopper freely tumbles without actuation. Practically, a robust control input for tumbling is simply the average of these upper and lower bounds.

## 2.3. Twisting Dynamics and Control

In addition to hopping and tumbling for mobility, another useful maneuver for changing orientation on the surface is a turn-in-place, or “twist” maneuver. Instead of using the flywheels to spin about a horizontal axis (i.e., for hopping and tumbling), the idea here is to spin about an axis *normal* to the surface such that the hopper rotates a desired angle,  $\psi_d$  (see Figure 5). The ability to control orientation could be extremely useful for pointing cameras and science instruments, or even to simply get in a more favorable configuration for a subsequent hop.

In the nominal resting configuration, the hopper is oriented such that three or four of its spikes are contacting the surface with one flywheel axis dominantly pointing “up.” Thus, a twisting maneuver can be executed with a single flywheel. Although the motors should be capable of applying the small torque required to initiate a twist, a more controllable and robust approach is to spin the flywheel up slowly



(such that the hopper does *not* rotate) and hit the brakes—similar to the hopping control strategy discussed in Section 2.1.1. Assuming the hopper is resting on a flat, inclined surface (angle  $\beta$ ) with a Coulomb friction contact model (i.e.,  $F_\mu = \mu_k F_N$ ) and a spike-to-spike base length of  $s$ , the resisting friction torque is given by  $\tau_\mu = -K_s s \mu_k m g \cos \beta$ , where the “mean contact radius”  $K_s = \sqrt{2}/2$  for a cube. This frictional torque corresponds to the maximum rate at which the flywheel can be accelerated prior to braking and the rate at which the hopper decelerates after braking. Conservation of angular momentum can again be invoked to derive an expression for the flywheel speed required to rotate an angle  $\psi_d$ :

$$\begin{aligned} \omega_f(\mu_k, \psi_d) &= \frac{I_p}{I_f} \sqrt{\frac{-2\tau_\mu \psi_d}{I_p}} \\ &= \frac{1}{I_f} \sqrt{(2I_p K_s s m g \cos \beta)(\mu_k \psi_d)}. \end{aligned} \quad (16)$$

This equation for the control input is written explicitly as a function of  $\mu_k$  to emphasize that it is strongly dependent on the surface friction—a parameter that is, in general, unknown *a priori*. However, an estimate for the friction parameter ( $\hat{\mu}_k$ ) can be refined by observing the response to a known input. In this way, a *sequence* of twist maneuvers can be executed until the desired precision in  $\psi_d$  is achieved, even in the presence of uncertainty and variability in the environment. Furthermore, the assumption of Coulomb friction on a smooth surface is not true in general, and there could even be cases in which the local terrain is so uneven that twisting causes the hopper to lose ground contact altogether. Equation (16) can be modified to account for other proposed contact models (e.g., adding a viscous damping term), but Coulomb friction is a simple *single-parameter* model that can capture a wide range of surface conditions.

### 3. HOPPER DESIGN

In this section, we briefly address system design considerations. Specifically, we first focus on the mobility system (the focus of this paper), and then we discuss integration into a complete, science-capable space system.

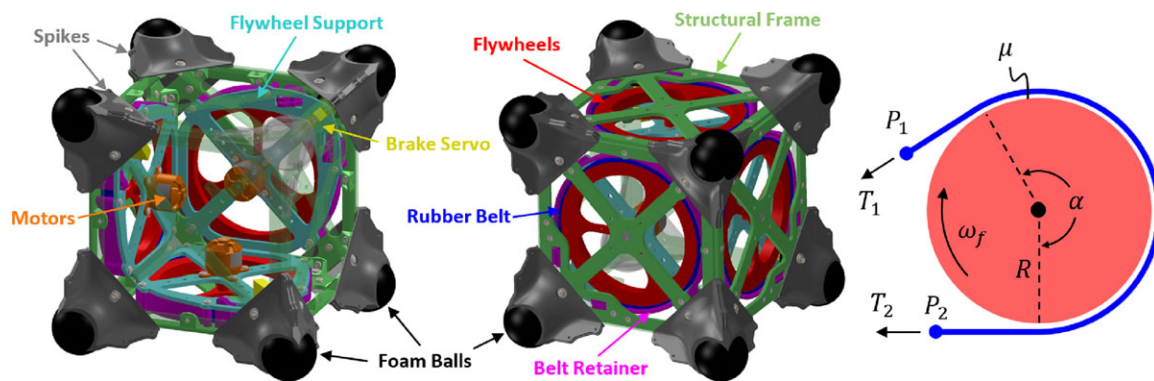
#### 3.1. Mobility System Design

First and foremost, the flywheels are one of the most important components of this rover concept. The shape, sizing, and placement of the flywheels represents an important trade space to consider, which is influenced by the target body of interest, the scale of mobility desired, and mass/space allocation requirements for other subsystems. For example, higher surface gravity requires more momentum to be generated for a given hop distance, as indicated by Eq. (6). One of the most important metrics to

consider is mobility *efficiency* [see Eq. (5)], which is highly dependent on the flywheel inertia. More precisely, the efficiency favors a high flywheel inertia *and* low total inertia—an inherent tradeoff because the mass and inertia of the flywheel also contribute to the total inertia. We have extensively studied the flywheel shape-optimization problem in the context of efficient mobility with mass and size constraints; the key finding is that efficiency favors dense, thin-rimmed, large diameter flywheels located as far from the CM as possible. Accordingly, the flywheels on our current prototype (which was designed to optimize efficiency for mobility in 1 g) are 5-in.-diam, steel rimmed disks with an inertia of 9,500 g cm<sup>2</sup> and mass of 300 g, or about 1/8th the total mass (see Figure 6, left).

Equally important to the flywheels are the actuators use to manipulate them—namely, motors and brakes. Because the motors are not directly responsible for mobility under the control regime proposed in Section 2, they can be arbitrarily small, solely constrained by the time required to build momentum and possibly by the torque requirements for in-flight attitude control. A direct-drive is the simplest approach, but geared or belt-driven couplings can also be implemented for more flexibility over motor placement. The prototype in Figure 6 has three 50 W brushless motors with Hall sensor feedback (Hobby People 2208/15) and electronic speed controllers (Emax BLHeli-12A).

The braking system requires special attention, as it is directly responsible for executing the motion primitives discussed in Section 2. We have experimented with various types of braking mechanisms, including friction disks and impulsive braking via impact hammers, but by far the most effective architecture utilizes a *band brake*, as illustrated in Figure 6, right. Consisting of a Kevlar-reinforced neoprene belt wrapped around the circumference of the flywheel, the band brake applies a friction-generated torque directly on the flywheel by pulling the belt taut. In the retracted state, the belt is robustly held against an outer, concentric retaining ring by small springs, which maintains a 1–2 mm radial clearance for the flywheel to freely rotate. The applied torque is governed by the well-known capstan equation,  $T_1 = T_2 e^{\mu \alpha}$  (for  $\omega_f > 0$ ), whereby the exponential gain ( $e^{\mu \alpha}$ ) allows very high torques [ $\tau = (T_1 - T_2)/R$ ] to be achieved for relatively low force inputs. Thus, this presents two possible forms of actuation: (i) *high* torque by pulling on  $P_2$  and fixing  $P_1$  to the frame, or (ii) *low* torque by pulling on  $P_1$  and fixing  $P_2$  to the frame (the reverse is true for CCW rotation). For our prototype, with a microservo motor (DSM44 by Power HD) generating tension up to 15 N,  $\alpha = 3\pi/2$ , and  $\mu \approx 1$ , option (i) can generate torques up to 100 Nm and option (ii) up to 1 Nm. Thus, this architecture has the capability of achieving a wide variety of hopping maneuvers (refer to Figure 3). Furthermore, it has proven to be robust, showing no appreciable signs of wear on the belt or structural degradation after hundreds of cycles.



**Figure 6.** Left: CAD model of prototype, annotating key components. Right: schematic of band brake mechanism.

The overall structure and frame consists of a cube with a 15 cm edge constructed out of lightweight laser-cut and 3D printed parts ( $m_p = 2.3$  kg,  $I_p = 0.013$  kg m<sup>2</sup>), and one spike on each corner. Previous prototype iterations have included more spikes (Allen et al., 2013), but it has been determined through experimentation and insights from dynamic analysis (see Section 2) that a cubic geometry with eight spikes offers the best balance of protection and mobility performance. Each spike is fitted with a rubber foam tip to mitigate impact stresses and increase surface friction. However, even for large hops over 100 m, the impact speeds are typically low ( $<1$  m/s) and structurally tolerable even without extensive padding. In other words, due to the typical *slow* dynamics in microgravity, repeated impacts do not generally pose structural concerns. Also, although not considered in the analysis of Section 2, a larger spike surface area has better performance in loose granular media.

### 3.2. System Architecture

A notional system design study has been performed to demonstrate how the mobility system could be integrated into a complete, science-capable spacecraft. While the spacecraft architecture can be scaled according to the desired payload and capabilities (anywhere from roughly 1 kg to over 100 kg), our current reference concept is a 25 cm cube with a mass of approximately 25 kg and payload allocation of 3 kg (see Figure 7, left). A system of this size was designed with respect to a notional mission to Phobos (or other bodies of similar size).

As a small platform, this concept benefits significantly from miniaturized avionics currently under development at JPL for the first set of interplanetary CubeSats<sup>3</sup> (JPL, 2015). These developments include the radiation-tolerant Sphinx Command & Data Handling (C&DH) board. Based on the LEON3-FT processing core, Sphinx possesses the re-

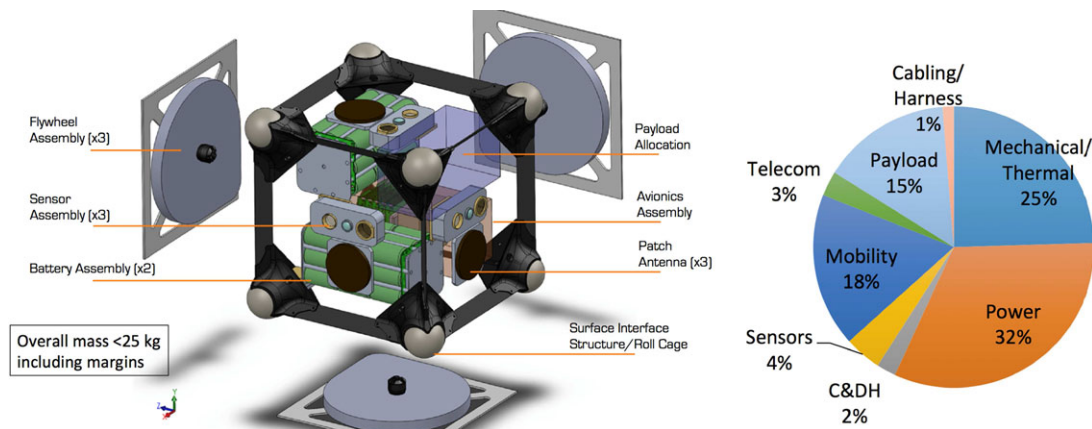
quired capabilities to support autonomous navigation and onboard image processing, which reduces the burden on the host mission and the need for frequent “ground-in-the-loop” operations.

Due to their scalability and relative simplicity, primary batteries were chosen as the power source for the reference concept. Although solar panels could be an option in some scenarios, practical concerns include limited surface area of the cubic configuration, resilience to impacts and dust, distance to the sun, as well as shadowed regions (e.g., craters or sinkholes) and diurnal cycles of potential target bodies. Approximately 5.4 kg of LiSOC12 batteries provide a total capacity up to 1,450 W-h (depending on average current draw and temperature), enabling the exploration of multiple sites over several Earth days.

A mass breakdown of the reference concept is shown in Figure 7, right. The system mass is dominated by batteries in order to maximize the mission duration and operational flexibility. However, battery size can easily be scaled or traded for additional payload or other resources, depending on the specific mission requirements. Significant structural mass has been allocated to accommodate the rigors of tumbling and bouncing on a rough planetary surface (even on microgravity bodies, initial deployment and drops from high altitudes may result in impacts of several g’s).


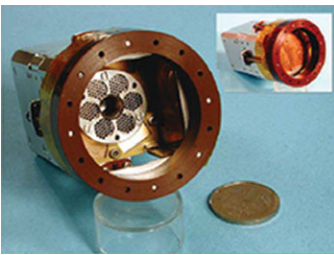
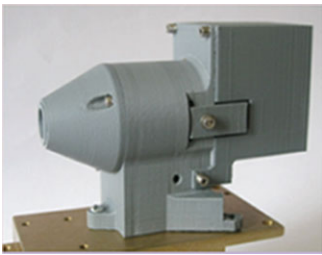
The hopping rover can achieve a broad range of scientific objectives by accommodating a variety of instruments, which benefit from recent advances in sensor and electronics miniaturization and packaging. In response to the Planetary Science Decadal Survey (NRC, 2011), investigations encompass elemental and mineralogical composition of the surface and physical characterization of the regolith [e.g., see Castillo Rogez, Pavone, Nesnas, Hoffman, et al. (2012)]. Investigations geared toward retiring strategic knowledge gaps for human exploration also include the quantification of surface electrostatic charging, dust dynamics, and the search for subsurface water. A reference payload includes a multispectral camera, the IntelliCam context imager developed for the Near Earth Asteroid Scout mis-

<sup>3</sup>Miniaturized satellites typically scaled by 10 cm cubic units, ranging from “1U” to “6U.”



**Figure 7.** Left: notional configuration for a reference mission to Phobos. Right: subsystem mass breakdown.

**Table II.** Example of representative payload for the *in situ* exploration of the surface composition and physical properties of a small body.

Instrument	IntelliCam	APXS	Microscope
Science objective	Context imaging surface navigation	Elemental composition	Regolith physical properties
Mass	500 gm	640 gm	500 gm
Power	2.5 W (peak)	1.5 W (peak)	2 W
			

sion (McNutt et al., 2014), a small alpha particle and x-ray spectrometer (APXS), such as flown on Rosetta Philae comet lander (Klingelhöfer, Brückner, Duston, Gellert, & Rieder, 2007), and the MicrOmega microscope developed for the Phobos-Grunt mission (Pilorget, Bibring, & Berthe, 2011). Mass and power specifications for these instruments are summarized in Table II. In addition to the science payload, a complement of accelerometers, sun sensors, star-field cameras, and wide-angle context cameras aid in localization and navigation, as well as providing context for science investigations.

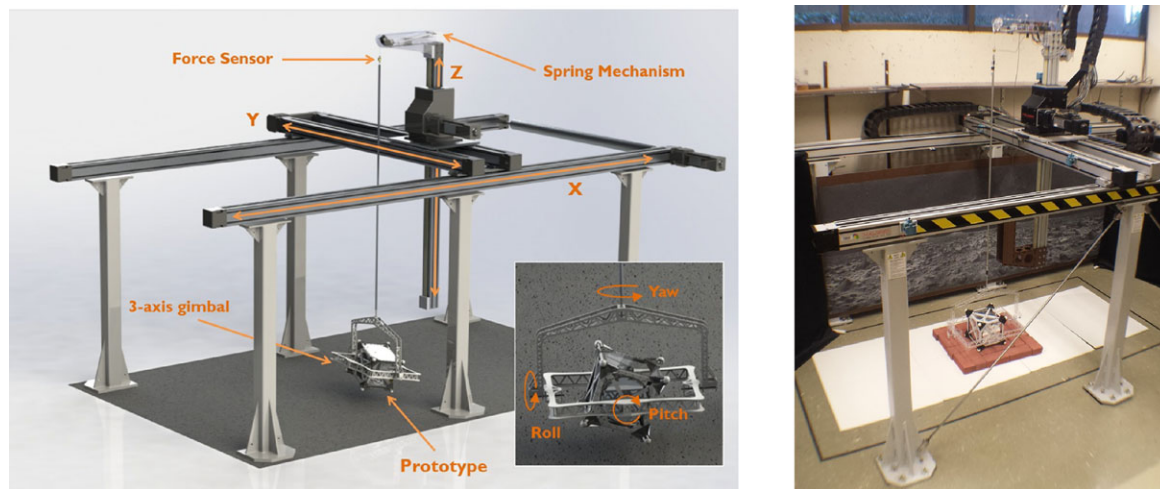
#### 4. MICROGRAVITY TEST BED

Earth-based validation of microgravity mobility platforms represents a major challenge. Parabolic flights and drop tower environments can offer periods of reduced effective gravity, but their use for long-duration and repeated testing is not possible due to the brevity of the microgravity peri-

ods (<20 s) and cost constraints. A grounded, experimental test bed is required for the *iterative process* of validating and improving the mobility performance of a microgravity mobility platform, in particular our hopper concept.

Methods for emulating microgravity environments are multifold. Allen et al. (2013) implemented a 3 DoF test bed consisting of a planar version of the hopper supported on a flat *inclined* granite table by frictionless air-bearings. This approach works well for emulating microgravity dynamics in two dimensions, but it is inherently unable to capture out-of-plane motions, which are critical for demonstrating *directional* control in a 3D world. One simple approach to allow for full 3D motion is by using a “gravity offloading” *Atwood machine* (Allen et al., 2013; Reid, Roveda, Nesnas, Pavone et al., 2014), which works by suspending the hopper by a cable looped over a pulley with a counterbalance acting to vertically offload most of the weight. However, these systems only allow for a restricted range of motion and introduce exogenous pendulum dynamics into the system.





**Figure 8.** Left: 6 DoF microgravity test bed CAD rendering. The powered gantry tracks the translational motion of the hopper in  $x$ ,  $y$ , and  $z$  within a volume of  $3\text{ m} \times 1\text{ m} \times 1\text{ m}$ , respectively, while allowing for free fall in  $z$  at sub-milli-g levels. The gimbal frame allows the hopper to rotate in all three axes. Right: image of the test bed.

There have been a few attempts to emulate 6 DoF microgravity motion within a larger workspace. A small legged rover was rigidly attached to the end of a multijointed manipulator arm, which used force-feedback impedance control to track the rover's motion (Chacin & Yoshida, 2008). A 6 DoF test bed was also developed at JPL for testing landing scenarios for a six-limbed rover concept, ATHLETE (Wilcox, 2012). Based on the concept of an inverted "Stewart platform," this test bed uses six controlled cable winches with force feedback to track motion in all 6 DoFs. However, these architectures only allow for a limited range of rotation, and they do not appear suitable for tracking fast motions—a critical requirement for abrupt hopping and bouncing.

To the best of our knowledge, no preexisting test beds are capable of meeting the stringent requirements for emulating the hopper's dynamics in microgravity: (i) effective gravity levels on the order of  $10^{-3}$  g's, (ii) allowing for full 6 DoF motion with (iii) minimal exogenous dynamic interference, (iv) over an extended period of time (say, more than 20 s), and (v) within an extended workspace (say, more than  $1\text{ m}^2$ ). ARGOS, a gravity offload system developed at NASA's Johnson Space Center, may come the closest (Valle, Dungan, Cunningham, Lieberman, & Poncia, 2011). Used primarily for human testing in zero-g environments, ARGOS consists of an actively controlled overhead three-axis gantry crane that tracks the motion of the suspended subject, enabling the "free-floating" behaviors observed in space. A similar gantry system, aimed at reproducing zero-gravity conditions, was developed at NASA's Ames Research Center for testing "Personal Satellite Assistants (PSAs)" (Niewarner & Dorais, 2006). At Stanford, we extended this idea to create a novel 6 DoF test bed for operating hoppers in *microgravity* conditions (see Figure 8).

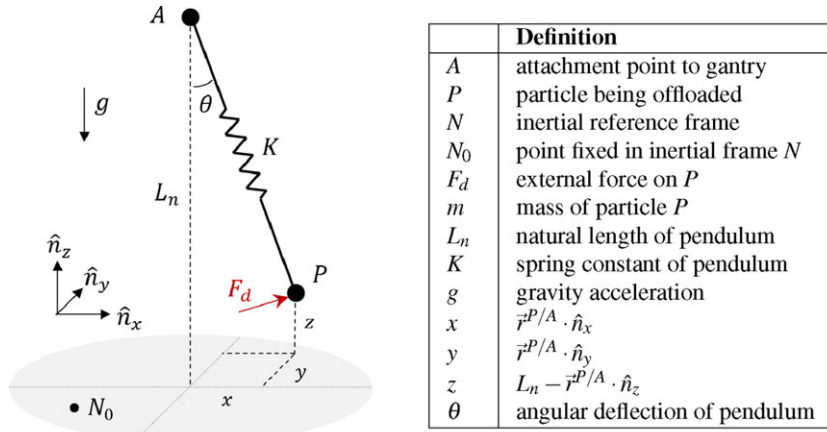
#### 4.1. Test Bed Design

Similar to ARGOS, our test bed is built on a powered gantry crane that permits the tracking of translational motion. The three-axis rotational motion of the hopper is achieved by mounting it within a lightweight rigid gimbal frame (see Figure 8). The gimbal-mounted hopper is suspended by a cable from an overhead attachment point on the gantry crane so that it can swing freely. By accurately measuring the relative deflection of the pendulum, the  $x$  and  $y$  axes are actuated using feedback control techniques to keep the pendulum in a vertical state. In this manner, external lateral forces that act on the hopper cause the whole system to accelerate, as Newton's second law predicts. To enable microgravity free fall, the control of the vertical axis utilizes force feedback with a series-elastic coupling to apply a precise offloading force on the hopper, even in the presence of external forces.

In the next sections, we discuss in detail the dynamics and control of the test bed. As mentioned above, the main tenet behind our approach is to decouple the translational and rotational motions of the hopper, just as the equations of motion inherently decouple for any unconstrained rigid body. In this way, the translational motion tracking problem can consider a simple particle, and the rotational problem can assume a fixed center of mass (CM), which greatly simplifies the control.

##### 4.1.1. Translational Tracking

The fundamental goal of translational tracking is to maintain a perfectly *constant* and *vertical* offloading force during long periods of slow drift (i.e., ballistic flight) and in response to large impulsive force inputs (i.e., ground



**Figure 9.** Dynamic model of the test bed. The hopper is modeled as a particle ( $P$ ) that is suspended from a control point on the gantry ( $A$ ) by an elastic pendulum of length  $L_n$  and stiffness  $K$ .

collisions). This motivates the use of passive elements such as springs and bearings, which have the benefit of instantly responding to external forces (as is the case with air-bearing-supported free flyers—the gold standard for *zero-gravity* 2D test beds). As an idealized example, consider a particle suspended by an infinitely long, massless constant-force spring. At any position in space, this particle would indeed be offloaded by a perfectly constant and vertical force. Practically, for our desired specs, this would require a pendulum over 1 km long and a force precision beyond the hysteresis and creep limitations of even the best springs. However, in the same vein as the ARGOS test bed, these passive benefits can be augmented with a powered three-axis gantry tracking system to provide larger area coverage with a reasonably sized pendulum and spring (see Figure 8).

Consider the dynamic model of the test bed in Figure 9. The hopper is modeled as a particle ( $P$ ) that is suspended from a control point on the gantry ( $A$ ) by an elastic pendulum of length  $L_n$  and stiffness  $K$ . Most generally, this system has 12 states,

$$\begin{aligned} \vec{r}^{P/N_0} &= \begin{bmatrix} x_P \\ y_P \\ z_P \end{bmatrix}, \quad \vec{r}^{A/N_0} = \begin{bmatrix} x_A \\ y_A \\ z_A \end{bmatrix}, \quad {}^N \vec{V}^P = \begin{bmatrix} \dot{x}_P \\ \dot{y}_P \\ \dot{z}_P \end{bmatrix}, \\ {}^N \vec{V}^A &= \begin{bmatrix} \dot{x}_A \\ \dot{y}_A \\ \dot{z}_A \end{bmatrix}, \end{aligned} \quad (17)$$

where  $\vec{r}^{P_1/P_2}$  denotes the position vector to point  $P_1$  from point  $P_2$ , and  ${}^N \vec{V}^P$  denotes the velocity of point  $P$  in frame  $N$ . However, the dynamics of  $P$  are governed only by the *relative* position with respect to  $A$ , so it is more convenient to collapse the state to six “relative” states:

$$\vec{x} = \begin{bmatrix} x \\ y \\ z \end{bmatrix} = L_n \hat{n}_z + \vec{r}^{P/N_0} - \vec{r}^{A/N_0}, \quad \dot{\vec{x}} = \begin{bmatrix} \dot{x} \\ \dot{y} \\ \dot{z} \end{bmatrix}. \quad (18)$$

Here,  $\vec{r}^{P_1/P_2}$  denotes the position vector to point  $P_1$  from point  $P_2$ , and  ${}^N \vec{V}^P$  denotes the velocity of point  $P$  in frame  $N$ . The full nonlinear dynamics of the system are given by

$$\ddot{\vec{x}} = \frac{-mg - K(L - L_n)}{mL} \vec{x} - g\hat{n}_z - \vec{u}, \quad L = \|\vec{r}^{P/A} - \vec{x}\|, \quad (19)$$

where the control input,  $\vec{u} = [u_x \ u_y \ u_z]^T = {}^N \vec{a}^A$ , is the acceleration of point  $A$ . The elastic pendulum is a classic example of a nonlinear system with coupled resonant modes. However, when regulated about the equilibrium, the dynamics can be linearized and fully decoupled. That is, if  $|x|, |y|, |z| \ll L_n$ , then  $\sin \theta \approx \theta$ ,  $\cos \theta \approx 1$ , and the dynamics can be written as

$$\begin{aligned} \begin{bmatrix} \dot{x} \\ \ddot{x} \end{bmatrix} &= \begin{bmatrix} 0 & 1 \\ -\frac{g}{L_n} & 0 \end{bmatrix} \begin{bmatrix} x \\ \dot{x} \end{bmatrix} + \begin{bmatrix} 0 \\ -1 \end{bmatrix} u_x, \\ \begin{bmatrix} \dot{y} \\ \ddot{y} \end{bmatrix} &= \begin{bmatrix} 0 & 1 \\ -\frac{g}{L_n} & 0 \end{bmatrix} \begin{bmatrix} y \\ \dot{y} \end{bmatrix} + \begin{bmatrix} 0 \\ -1 \end{bmatrix} u_y, \\ \begin{bmatrix} \dot{z} \\ \ddot{z} \end{bmatrix} &= \begin{bmatrix} 0 & 1 \\ -\frac{K}{m} & 0 \end{bmatrix} \begin{bmatrix} z \\ \dot{z} \end{bmatrix} + \begin{bmatrix} 0 \\ -1 \end{bmatrix} u_z. \end{aligned} \quad (20)$$

This decoupling greatly simplifies the tracking control to that of three independent spring-mass systems (negligible damping), for which classical linear control design techniques can be readily applied (i.e.,  $\vec{u} = -K\vec{x}$ ). The control variable  $\vec{u} = {}^N \vec{a}^A$  assumes direct control of the gantry acceleration, which indeed can be achieved with a much tighter motor control loop up to some  $\vec{u}_{\max} = [a_{x\max} \ a_{y\max} \ a_{z\max}]^T$ , reflecting the fundamental limitation of the motors to accelerate an inertial load. For our gantry,  $\vec{u}_{\max} = [4 \ 6 \ 10]^T$  (m/s<sup>2</sup>). Thus, tracking the particle  $P$  that has been subject to larger accelerations (e.g., through collisions with the environment) will inherently incur transient error. This is precisely why the series-elastic coupling between  $P$  and  $A$  is critical—it allows for larger relative motion about the equilibrium, which reduces the force error according to Hooke’s



law. Moreover, assuming maximum control inputs are used to respond to an *impulse* force input on  $P$ , it can be shown that the force error incurred is proportional to the spring constant of the system ( $K$  for the vertical axis and  $g/L_n$  for the lateral axes), thus reiterating the benefit of a *longer pendulum* and a *lower spring constant*. Our system has a 2-m-long pendulum with a spring constant of 5 N/m, which corresponds to natural frequencies of 0.35 and 0.2 Hz in the lateral and vertical axes, respectively. A low-stiffness spring/cam pulley system provides vertical compliance, as described in Duval (2010).

The very low target gravity level (0.001 g) also imposes demanding requirements on the state estimation. In the vertical axis, a precision force sensor (Futek LSB200) measures the cable tension to a resolution below 0.0001 (i.e., 0.1 g per kg)—sufficient to regulate at 0.001 g with less than 10% error. A custom sensor was designed to achieve comparable precision for sensing lateral deflections (i.e.,  $\delta x, \delta y \leq 200 \mu\text{m}$  resolution for a 2 m pendulum, or  $\delta\theta \leq 20$  arcsec). Based on the principle of differential inductive sensing, this sensor works by using strategically placed inductive pick-up circuits to measure the strength of the ac current-induced magnetic field emitted by the suspension cable, and thus its deflection due to  $1/r$  dissipation of the field. This sensor has a range of several centimeters, a resolution below  $100 \mu\text{m}$ , and it uses geometry-based signal processing to decouple  $x$  and  $y$  deflections. Collectively, these sensors provide sufficient state estimation precision to achieve emulated gravity levels below 0.0005 g's (approaching that of Phobos and larger asteroids) with a control loop running at 100 Hz. Practically, filtering techniques can be implemented to further reduce the attainable gravity, but at the cost of slower dynamic response.

#### 4.1.2. Rotational Tracking

Just as the translational problem considered the hopper as a particle, rotational tracking will assume a fixed CM. The problem then is how to hold the CM fixed while allowing for 3D rotation with minimal exogenous dynamics. Traditionally, spacecraft and control moment gyroscopes are mounted within three-axis gimbal frames for testing attitude control systems on Earth. Due to its symmetric geometry, a gimbal also provides a natural way to “attach” the hopper to the test bed, allowing it to rotate about any arbitrary axis (see Figure 8, left). Just as translational tracking attempts to preserve  $F = ma$  (see Section 4.1.1), rotational tracking should ideally preserve  $M = dH/dt$  (of the unconstrained hopper). However, in general, momentum is not conserved within a *massive* gimbal that passively rotates, nor is the total angular momentum of the entire *system*—momentum can be exchanged between the hopper and the gimbal itself, or dissipated through moments applied at the attachment to the inertial frame. In principle, an active series-elastic control of each gimbal axis could help to solve

this problem (as was done for the translational tracking), but this would require cumbersome motors that are both heavy and difficult to implement and control. Instead, a closer look at the dynamics of the passive gimbal system can show that there are many cases for which the hopper's dynamics remain relatively undisturbed, and indeed, many of the cases we care about for mobility.

Consider the dynamic model of the passive gimbal system in Figure 10. Recall that for a well-regulated translational system (i.e., small deflections) and a symmetric gimbal (i.e., the CM is in-line with the pendulum), the dynamics decouple, allowing this rotational problem to be analyzed in isolation. The system dynamics are governed by<sup>4</sup>

$$\begin{aligned} \vec{M}^S &= \frac{N}{dt} \vec{H}^S, & N \vec{H}^S &= N \vec{H}^A + N \vec{H}^B + N \vec{H}^C \\ &+ \sum_{k=x,y,z} N \vec{H}^{F^k}, \end{aligned} \quad (21)$$

$$\begin{aligned} N \vec{H}^A &= \vec{I}^A \cdot N \vec{\omega}^A, & N \vec{H}^B &= \vec{I}^B \cdot N \vec{\omega}^B, & N \vec{H}^C &= \vec{I}^C \cdot N \vec{\omega}^C, \\ N \vec{H}^{F^k} &= \vec{I}^{F^k} \cdot N \vec{\omega}^{F^k}, \end{aligned} \quad (22)$$

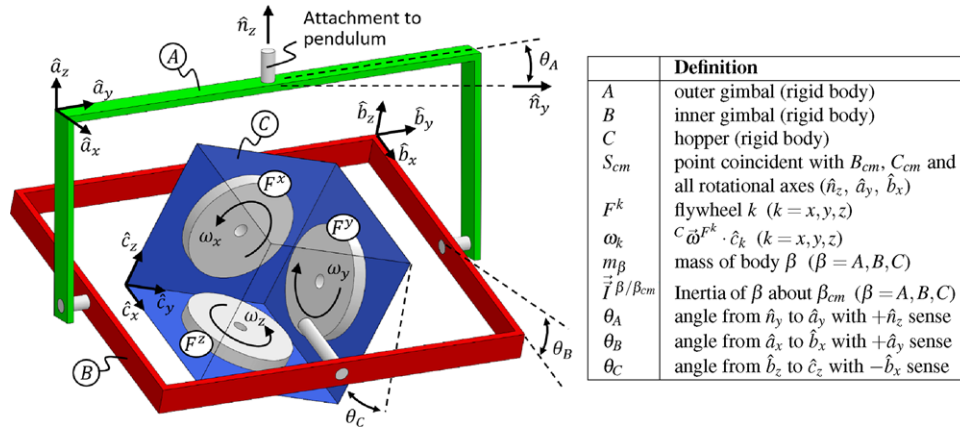
$$\begin{aligned} N \vec{\omega}^A &= \dot{\theta}_A \hat{n}_z, & A \vec{\omega}^B &= \dot{\theta}_B \hat{a}_y, & B \vec{\omega}^C &= -\dot{\theta}_C \hat{b}_x, \\ C \vec{\omega}^{F^k} &= \omega_k \hat{c}_k, \end{aligned} \quad (23)$$

$$\begin{aligned} N \vec{\omega}^B &= N \vec{\omega}^A + A \vec{\omega}^B, & N \vec{\omega}^C &= N \vec{\omega}^B + B \vec{\omega}^C, \\ N \vec{\omega}^{F^k} &= N \vec{\omega}^C + C \vec{\omega}^{F^k}. \end{aligned} \quad (24)$$

Note that these equations are in mixed bases, separated by up to three simple frame rotations. To solve for the dynamics explicitly in terms of  $\ddot{\theta}_A, \ddot{\theta}_B, \ddot{\theta}_C$ , they must be expressed in a single basis. Written out in their most general form, these equations are quite involved and not particularly useful. However, in order to study the behavior of the motion primitives discussed in Section 2, the full state evolution is not as important as the resulting trajectory. In other words, a more relevant question to ask is, “Given some desired trajectory, can the control input to the flywheels ( $\vec{\tau}_F$ ) be adjusted to account for the exogenous dynamics introduced by the gimbal?” Accordingly, the following analysis will characterize the additional angular momentum provided by the gimbal, which can then be compensated for by augmenting the control input.

Due to the high-friction brakes, the assumption of instantaneous momentum transfer can again be leveraged (i) to eliminate the gyroscopic effect of rotating flywheels as the hopper rotates, and (ii) for hopping, to assume ground contact is lost immediately upon actuation. Point (i) allows  $C$  and  $F$  to be treated as a single rigid body (say,  $D$ ), and (ii) collapses the state evolution of interest to that of a single state—the *resting state*. Thus, for any given resting state  $(\theta_A, \theta_B, \theta_C)$ ,

<sup>4</sup>Unless otherwise noted, all angular momentum and inertia are assumed to be about  $S_{CM}$ .



**Figure 10.** Dynamic model of the hopper within a passive three-axis gimbal frame. The hopper (C) can freely rotate about a single axis with respect to the inner gimbal frame (B), which in turn can freely rotate with respect to the outer gimbal frame (A) about an orthogonal axis. The outer gimbal can freely rotate about the vertical axis (i.e., along the pendulum), and all three rotational axes intersect with the CM of all bodies ( $S_{CM}$ ).

the total angular momentum of the system ( ${}^N\vec{H}^S$ ) required to generate the desired spin ( ${}^N\vec{\omega}^D$ ) can be compared to that of the unconstrained hopper ( ${}^N\vec{H}^D$ ) according to the formulas

$$\begin{aligned}
 {}^N\vec{H}^S &= I_z^A \dot{\theta}_A \begin{bmatrix} -\sin \theta_B \\ -\cos \theta_B \sin \theta_C \\ \cos \theta_B \cos \theta_C \end{bmatrix}_c \\
 &+ \begin{bmatrix} I_x^B \dot{\theta}_A \sin \theta_B \\ I_y^B \dot{\theta}_B \cos \theta_C - I_z^B \dot{\theta}_A \cos \theta_B \sin \theta_C \\ I_y^B \dot{\theta}_B \sin \theta_C + I_z^B \dot{\theta}_A \cos \theta_B \cos \theta_C \end{bmatrix}_c \\
 &+ \begin{bmatrix} I_x^D (-\dot{\theta}_C - \dot{\theta}_A \sin \theta_B) \\ I_y^B \dot{\theta}_B \cos \theta_C - I_z^B \dot{\theta}_A \cos \theta_B \sin \theta_C \\ I_y^B \dot{\theta}_B \sin \theta_C + I_z^B \dot{\theta}_A \cos \theta_B \cos \theta_C \end{bmatrix}_c, \quad (25)
 \end{aligned}$$

$$\begin{aligned}
 {}^N\vec{H}^D &= \begin{bmatrix} I_x^D & 0 & 0 \\ 0 & I_y^D & 0 \\ 0 & 0 & I_z^D \end{bmatrix} \begin{bmatrix} \omega_x^D \\ \omega_y^D \\ \omega_z^D \end{bmatrix}_c \\
 &= \begin{bmatrix} I_x^D (-\dot{\theta}_C - \dot{\theta}_A \sin \theta_B) \\ I_y^D (\dot{\theta}_B \cos \theta_C - \dot{\theta}_A \cos \theta_B \sin \theta_C) \\ I_z^D (\dot{\theta}_B \sin \theta_C + \dot{\theta}_A \cos \theta_B \cos \theta_C) \end{bmatrix}_c. \quad (26)
 \end{aligned}$$

Equation (26) can be rearranged to express  $\dot{\theta}_k$  in terms of  $\omega_x^D$ ,  $\omega_y^D$ ,  $\omega_z^D$ , and then substituted into Eq. (25) to solve for the system's angular momentum as a function of  ${}^N\vec{\omega}^D$ ,

$${}^N\vec{H}^S = \begin{bmatrix} I_x^D & \tan \theta_B \sin \theta_C (I_x^B + I_z^A) & -\tan \theta_B \cos \theta_C (I_x^B + I_z^A) \\ 0 & \cos^2 \theta_C (I_y^D + I_y^B) + \sin^2 \theta_C (I_x^D + I_z^B + I_z^A) & \sin \theta_C \cos \theta_C (I_y^D + I_y^B - I_x^D - I_z^B - I_z^A) \\ 0 & \sin \theta_C \cos \theta_C (I_y^D + I_y^B - I_x^D - I_z^B - I_z^A) & \cos^2 \theta_C (I_z^D + I_z^B + I_z^A) + \sin^2 \theta_C (I_y^D + I_y^B) \end{bmatrix} \begin{bmatrix} \omega_x^D \\ \omega_y^D \\ \omega_z^D \end{bmatrix}_c. \quad (27)$$

This equation can be thought of as the “effective inertia” ( $\vec{I}^{S/SCM}$ ) of the hopper/gimbal system, which is a function of the state angles ( $\theta_A$ ,  $\theta_B$ ,  $\theta_C$ ) and inertias ( $\vec{I}^A$ ,  $\vec{I}^B$ ,  $\vec{I}^D$ ). Note that products of inertia are small and can be ignored due to the symmetric geometry. For a massless gimbal and symmetric hopper (i.e.,  $I_x^D = I_y^D = I_z^D$ ), Eq. (27) indeed collapses to Eq. (26), as expected. A special case of particular interest for mobility from a flat and level resting orientation (i.e.,  $\theta_A$ ,  $\theta_B$ ,  $\theta_C \approx 0$ ) greatly simplifies the effective inertia,

$${}^N\vec{H}^S|_{\theta_A, \theta_B, \theta_C=0} = \begin{bmatrix} I_x^D & 0 & 0 \\ 0 & I_y^D + I_y^B & 0 \\ 0 & 0 & I_z^D + I_z^B + I_z^A \end{bmatrix} \begin{bmatrix} \omega_x^D \\ \omega_y^D \\ \omega_z^D \end{bmatrix}_c. \quad (28)$$

In this case, all frames are aligned ( $\hat{n}_i = \hat{a}_i = \hat{b}_i = \hat{c}_i$ ) and the principal moments of inertia simply add. Indeed, it makes sense intuitively that a yaw maneuver, for example, must account for the inertia of both the outer and inner gimbals about  $\hat{n}_z$ , or that a hop about the  $\hat{n}_y$  axis must account for the inertia of the inner gimbal about  $\hat{n}_y$ . To observe the effect this has on the required control input, recall the generalized control for oblique hops given by Eq. (8), which maps the desired hopper rotation about spike tip  $P$  after braking to the required flywheel momentum prior to braking. In the test bed, the additional mass and effective

inertia of the gimbal can be compensated for with a simple change:

$$\left( \sum_{k=x,y,z}^N \tilde{H}^{F^k} \right) \Big|_{t=0^-} = \left( \tilde{I}^{S/SCM} + (m_D + m_A + m_B) \right. \\ \left. \cdot [(\tilde{r}^{P/D_{CM}} \cdot \tilde{r}^{P/D_{CM}}) \mathbf{I} - (\tilde{r}^{P/D_{CM}})(\tilde{r}^{P/D_{CM}})^T] \right) \cdot {}^N \tilde{\omega}^D \Big|_{t=0^+}. \quad (29)$$

In summary, the passive gimbal introduces additional effective mass and inertia to the hopper. The resulting additional angular momentum [Eq. (27)] can be accounted for by augmenting the control input based on Eq. (29), so that an “unconstrained” desired maneuver can be effectively emulated.

A fundamental limitation of the passive gimbal is its inability to preserve angular momentum in ballistic flight. The only two stable cases for which angular momentum is perfectly conserved are pure rotation about  $\hat{n}_z$  or  $\hat{c}_x$ , which conveniently corresponds to yaw maneuvers and single-axis hops. Angular momentum about any other arbitrary axis tends to result in large fluctuations or even chaotic momentum shifts as the gimbal becomes “locked” (i.e.,  $\hat{c}_x = \pm \hat{n}_z$ ). Also, the roll axis is partially constrained to avoid ground contact with the gimbal itself.

Another important consideration with such a gimbal is to ensure that the CM is precisely aligned with all rotation axes. Otherwise, it will rock like a pendulum rather than freely rotate. This requires adding dead-mass to the hopper to geometrically center the CM and a rigid gimbal that does not deflect under the weight of the hopper (thus causing the CM to “sag”). Clearly this is not a requirement for operation in true microgravity (i.e., on an asteroid) where the hopper is no longer suspended. In this case, the control analysis in Section 2.1.1 (which assumed a geometrically centered CM) can be modified to account for an offset CM by simply reshaping the rimless wheel geometry to reflect the asymmetric mass distribution. In other words, the lengths ( $l_i$ ) and angular spacing ( $\alpha_i$ ) of the spikes would need to be adjusted such that the spike tips remain fixed and the disk center is coincident with the true CM (refer to Figure 2). While an offset CM does not inherently limit the hopper’s capabilities, it does affect its trajectory (angle, speed, and distance). Thus, the control law for a hopper with an asymmetric mass distribution would need to be cognizant of orientation. In practice, the subsystems (e.g., batteries, avionics boards, etc.) can be strategically arranged to roughly center the CM, allowing the simpler, orientation-agnostic control laws developed in Section 2 to be used.

## 4.2. Test Bed Validation

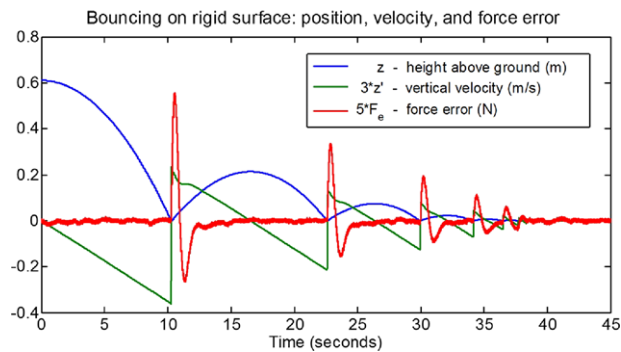
The test bed was first examined in the absence of external forces by performing reference drop and lateral ma-

neuvers. Specifically, drop tests with only vertical actuation exhibit a very strong parabolic fit (correlation typically above 99%), and the noise floor on the force sensor feedback allows for effective gravity levels down to about 0.0005 g’s. The lateral motion also behaves precisely as predicted without force input, remaining stationary or in a constant velocity. However, there is a small amount of drift in the signal from the lateral sensors (roughly 0.0001 g’s/min), which is handled with periodic recalibration before experiments. Interestingly, the lateral signal can be intentionally biased to “tilt the gravity vector off vertical,” producing an effectively inclined surface. Collectively, the lateral and vertical controls are highly effective at tracking parabolic trajectories.

A more careful analysis is required to validate the test bed’s response to external forces, which can be either impulsive or nonimpulsive. As a first test, a constant lateral force was applied to the hopper (mass  $m_p$ ) mounted on the test bed with a horizontal string looped over a pulley with a known mass  $m_t$  suspended. After initial transients settle, the system tracks the expected acceleration [ $a = gm_t/(m_p + m_t)$ ] to within 5%. A similar test was performed in the vertical axis by simply adding small amounts of known mass to the hopper, which also produced accelerations in close agreement with theoretical predictions (to within 1%).

Characterizing the behavior under impulsive forces is more challenging. First of all, the elasticity of a collision depends on many factors (e.g., properties of contacting materials, speed of impact, geometry of deformation, etc.), making it impractical to characterize theoretically as a basis for comparison. However, as a preliminary test, a proof mass (equal to the mass of the prototype) was mounted on the test bed and dropped onto an elastic surface (basically a webbing of rubber surgical tubing acting as a trampoline)—a contrived, low-stiffness interface that dissipates very little energy. In drop tests at 0.001 and 0.005 g’s, the mass was released from rest at a height of roughly 1 m, and it did indeed recover about 90% of its energy after each subsequent collision (number of trials = 36, mean = 91.5%, and standard deviation = 2.7%).

For collisions with stiffer or even rigid surfaces, energy dissipation is much more difficult to predict. However, the deviation observed in the force signal during impact is a good indicator of fidelity. Figure 11 reports the vertical height and velocity of the proof mass during an example drop/bouncing sequence on a rigid surface, as well as the transient force errors. Although the gantry overshoots vertical position by up to a few inches after a collision, the low stiffness of the spring mechanism ( $\approx 5$  N/m) results in transient force errors within a few hundred milli-Newtons—less than 1% of the proof mass’ weight. Since the force error scales roughly linearly with impact speed, there is an upper bound at which the transient response becomes unacceptable, putting the ideal range of operation between 0.0005 and 0.005 g’s.



**Figure 11.** Experimental results from bouncing on a rigid surface at 0.001 g's: height and velocity of test mass and error in vertical offloading force. Data are sampled at 10 kHz and the control loop runs at 100 Hz. Note that data are scaled to fit on the same axes (see the legend for scaling and units).

## 5. MOBILITY EXPERIMENTS

To further characterize the dynamics and *controllability* of the hopper and to validate the models presented in Section 2, various experiments were conducted on the micro-gravity test bed. Specifically, trajectory data were collected while performing (i) hops about a single axis, (ii) oblique hops over a single spike, and (iii) twisting maneuvers. The position feedback from the gantry was used in conjunction with the force and displacement signals to determine the translational trajectory of the hopper. At this time, no measurements of orientation are taken, which is sufficient for comparison with the translational trajectory predictions from Section 2. However, encoders on the gimbal axes or visual tracking techniques could be implemented in future experiments to achieve accurate pose estimates. Here, we also restrict our study to maneuvers on a flat and level surface, leaving mobility on rough and uneven surfaces for future work. The surface material was a rigid tile, and the friction between it and the rubberized spike tips was high enough to prevent slip during hopping. To the best of the authors' knowledge, these results represent the first validation of controlled (albeit limited) mobility in a representative microgravity environment.

### 5.1. Single-axis Hopping

As a first set of experiments, simple hopping and tumbling maneuvers were executed about a single axis as a basis for comparison with the 2D analytical model from Section 2.1.1. To minimize the effect of exogenous gimbal dynamics (see Section 4.1.2), the axis of rotation was aligned with  $\hat{c}_x$  (see Figure 10), such that nominally the gimbal does not rotate and only the added mass must be accounted for according to Eq. (29). The initial orientation about the yaw axis was also set so that the hopper was "facing" along the gantry's  $x$  axis, allowing for independent measurement of out-of-

plane motions (i.e., along the  $y$  axis). In each experiment, the control approach discussed in Section 2.1.1 was executed, whereby the flywheel is slowly accelerated until a target angular velocity is reached, at which point the band brake is applied and the hopping sequence ensues unactuated. For a desired hop distance of 1 m in an emulated gravity level of 0.001 g's, the target flywheel velocity was calculated using Eq. (6) to be 550 rpm. A total of 30 single-axis hops were executed, 10 of which are plotted in Figure 12.

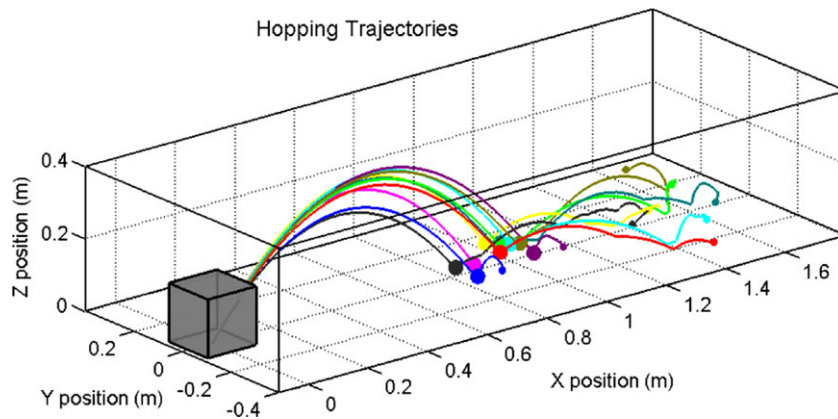
An interesting observation from Figure 12 is the variability in bouncing. Although the "landing envelope" for the first bounce is relatively small, subsequent trajectories are highly sensitive to the spin and orientation on impact, which results in a much wider "resting envelope." Recall, however, from Section 4.1.2 that the hopper's rotational dynamics are corrupted by the gimbal in flight, so these bouncing trajectories do not exactly capture the "true" expected distribution. On the other hand, hopping angle and distance measurements exhibit a more consistent trend and are in close agreement with the predictions of Eqs. (7) and (4). The mean hop angle for the 30 experiments was  $50^\circ$  with a standard deviation of  $3^\circ$ . This is marginally higher than the  $45^\circ$  prediction, likely due to the elastic rebound of the spike tip. Indeed, numerical simulations with a spring/damper contact model also exhibit higher hop angles. Remarkably, without any adjustments in the model parameters, the mean hop distance of 0.94 m was also very close to the target of 1 m, with a standard deviation of 0.07 m. Here, the variability likely comes from imperfect control of the flywheel's speed and variability in the hop angle. Finally, as expected for single-axis hops, only minor deviations in heading were observed, with a mean of just  $1.5^\circ$  and a std. dev. of  $2^\circ$ . See Appendix for a sample video of a hopping experiment.

### 5.2. Oblique Hopping

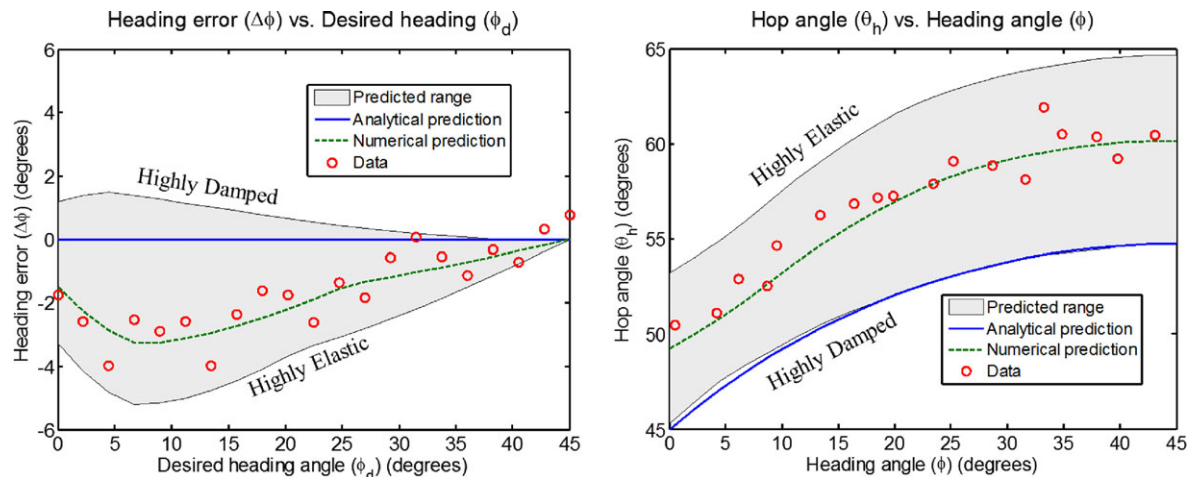
A similar set of experiments was performed to demonstrate directional control by hopping over a single spike, as discussed in Section 2.1.2. In this case, the flywheel speeds were calculated based on Eq. (8) and augmented to account for the gimbal's effective mass and inertia governed by Eq. (29). Twenty hops were executed over a range of desired heading angles ( $0 \leq \phi_d \leq 45^\circ$ ) and at a nominal speed of 5 cm/s (which corresponds roughly to a 1 m hop). The observed heading ( $\phi$ ) and hop ( $\theta_h$ ) angles are compared with predictions based on the analytical model from Section 2.1.2 and with simulated trajectories based on a spring/damper contact model (see Figure 13). The "predicted range" is derived from numerical simulations, and it highlights the trajectory variability that can be induced by changes in the surface contact model, ranging from highly damped to purely elastic. Numerical results from a "best-fit" surface contact model are also indicated by the green dashed line.

Figure 13 (left) illustrates that, overall, the directional control law is highly effective at achieving the desired head-





**Figure 12.** Trajectories of the hopper within the microgravity test bed. The gravity level of these experiments was set to 0.001 g's, and the flywheel was commanded to 550 rpm. Position data for each experiment were shifted to start at the origin. A  $z$  position of zero corresponds to a flat stance where four spikes are in contact with the ground. Thus, bounces above zero indicate collision at a tilted orientation. Initial bounces are highlighted with a large point, and the final resting location is indicated with a smaller point.



**Figure 13.** Oblique hops were executed over a range of desired heading angles and compared with predictions based on analytical and numerical models. Left: The error in heading angle ( $\Delta\phi$ ) as a function of intended heading angle ( $\phi_d$ ). Right: Hop angle ( $\theta_h$ ) as a function of intended heading angle.

ing angle, with a mean deviation of only  $2^\circ$ . Furthermore, the data and simulations both indicate a bias toward *undershooting* the intended heading, which can be corrected for with a simple shift in the control law. Nonetheless, even heading deviations up to  $10^\circ$  (say) still constitute a stark improvement in directional control over single-axis hops.

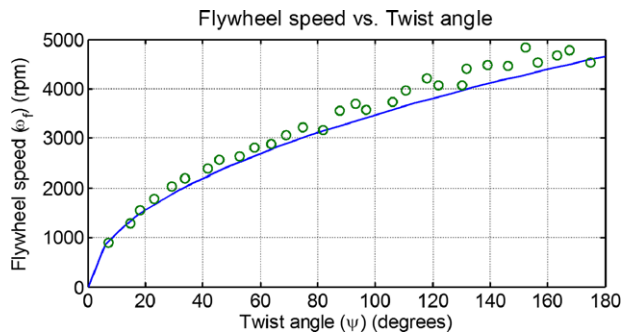
The hop angle data shown in Figure 13 (right) follows the trend predicted by Eq. (9) and also reiterates the observation from the single-axis hop experiments: surface elasticity increases the hop angle. Indeed, a sweep of numerical simulations shows that  $\theta_h$  can vary by up to  $10^\circ$  depending on the contact elasticity, whereby the lower bound corresponds to a highly damped surface and strongly agrees with the analytical model. Although the surface proper-

ties of small bodies may be highly variable, for a rigid surface the contact elasticity is predominantly governed by the compliance of the spike tip itself, which may be roughly characterized *a priori* and incorporated into the predictive model.

### 5.3. Twisting Experiments

Unlike hopping and tumbling, a twist is the only motion primitive that is not critically enabled by microgravity, as the CM (nominally) remains fixed. Thus, Eq. (16) should work equally well to predict the response in a 1 g environment, and the microgravity test bed is not needed. So the hopper was simply placed on a flat and level tile surface, and





**Figure 14.** A series of 30 twist maneuvers were executed over target range of  $0 < \psi_d < 180$ .

the friction coefficient was first estimated from a number of sliding force measurements to be  $\mu_k = 1.1$ . Equation (16) was then used to calculate the required flywheel speed to achieve a range of target twist angles ( $0 < \psi_d < 180$ ) based on the empirically determined  $\mu_k$  and measured hopper parameters. The results in Figure 14 show a very strong agreement with the predictive model, whereby the slight shift in the data could be attributed to any combination of imperfect estimates in the model parameters.

#### 5.4. Discussion

Collectively, the preliminary set of experiments presented here serve to cross-validate our analytical and numerical models, and indeed exhibit strong agreement. However, the surface conditions imposed here are admittedly contrived in order to best fit the modeling assumptions. On any small body, it is unlikely that a hopper would ever encounter terrain that exactly matches the flat and level tile surface used here. Specifically, there are two primary surface characteristics that may influence the performance of these motion primitives: (i) topography and (ii) structure. For the case of (locally) irregular topography, the hopper would typically only rest on three of its four base spikes, which could potentially incur large trajectory deviations when hopping with respect to the flat-ground case. A granular or deformable surface structure could also induce trajectory deviations.

While various surface properties certainly need to be addressed in future work, the analytical and experimental results for the simplified case may serve as a baseline for control on less idealistic surfaces. Moreover, it may often be difficult or impossible for the hopper to assess the properties of the surface upon which it is resting, in which case a surface-agnostic control regime is the only option.

We emphasize, however, that the ultimate goal is to reach targeted destinations, and accurately executing motion primitives is simply one factor that enables this. Figure 12 illustrates that, even for well-controlled hops, there is still a large degree of randomness incurred in the bouncing/settling process. Therefore, it may be more important to

be able to characterize and predict the *distribution* of landing states, or “landing envelopes,” than it is to refine the hopping precision. Future work will also consider methods of estimating landing envelopes in the context of motion planning.

## 6. CONCLUSIONS

In this paper, we have presented a planetary mobility hopper that uses internal actuation to achieve controlled maneuvers for long excursions (by hopping) and short, more precise traverses (by tumbling) in low-gravity environments. We have characterized the dynamics of such hoppers using angular momentum arguments, and we developed hybrid control strategies for mobility. We have also presented a prototype design and preliminary system architecture for a Phobos reference mission. Finally, the design and control of a first-of-a-kind 6 DoF microgravity test bed was also proposed, which has been used to validate control techniques for various motion primitives. Experimentation is ongoing, but the preliminary results constitute the first successful demonstration of *controlled* hopping mobility in such a high-fidelity test bed.

This paper leaves numerous important extensions open for further research. First, it is important to develop more realistic contact models for interactions with loose, granular media typically found on small bodies. Second, we seek to extend the control algorithms to reliably maneuver on uneven terrains and leverage them for higher-level motion planning objectives. Third, from a navigation perspective, we plan to develop localization techniques suited for the unique and challenging environments of small bodies, and for the constantly rotating motion of the hopper. Finally, future experiments will include (i) various surface characteristics such as inclination, rocks, sand, and fine powder, and (ii) tests of the closed-loop system integrating planning, control, and navigation.

## ACKNOWLEDGMENTS

The research described in this paper is supported by NASA under the Innovative Advanced Concepts program (Grant No. NNX14AT49G). The authors wish to acknowledge insightful discussions with Dr. J. C. Castillo (JPL), Dr. C. Zuffada (JPL), Dr. T. Cwik (JPL), Dr. J. Zmuidzinas (JPL), and B. Wilcox (JPL). Government sponsorship acknowledged.

## APPENDIX A: INDEX TO MULTIMEDIA EXTENSION

Extension	Media Type	Description
1	Video	An example hopping trajectory from the experiments described in Section 5.1

## REFERENCES

- Allen, R., Pavone, M., McQuin, C., Nesnas, I. A. D., Castillo Rogez, J. C., Nguyen, T.-N., & Hoffman, J. A. (2013). Internally-actuated rovers for all-access surface mobility: Theory and experimentation. In *Proceedings of the IEEE Conference on Robotics and Automation* (pp. 5481–5488), Karlsruhe, Germany.
- Castillo Rogez, J. C., Pavone, M., Nesnas, I. A. D., & Hoffman, J. A. (2012). Expected science return of spatially-extended in-situ exploration at small solar system bodies. In *IEEE Aerospace Conference* (pp. 1–15), Big Sky, MT.
- Chacin, M., & Yoshida, K. (2008). A microgravity emulation testbed for asteroid exploration robots. In *Proceedings of i-SAIRAS*.
- Decadal Survey Vision and Voyages for Planetary Science in the Decade 2013–2022. (2011). Technical report, National Research Council. Available at <http://solarsystem.nasa.gov/2013decadal/>.
- Dietze, C., Herrmann, F., Kuß, S., Lange, C., Scharringhausen, M., Witte, L., van Zoest, T., & Yano, H. (2010). Landing and mobility concept for the small asteroid lander MASCOT on asteroid 1999 JU3. In *61st International Astronautical Congress*.
- Duval, E. F. (2010). Dual pulley constant force mechanism. US Patent 7,677,540.
- Fiorini, P., & Burdick, J. (2003). The development of hopping capabilities for small robots. *Autonomous Robots*, 14(2), 239–254.
- Gajamohan, M., Merz, M., Thommen, I., & D'Andrea, R. (2012). The Cubli: A cube that can jump up and balance. In *IEEE/RSJ International Conference on Intelligent Robots and Systems* (pp. 3722–3727). IEEE.
- Glassmeier, K.-H., Boehnhardt, H., Koschny, D., Kührt, E., & Richter, I. (2007). The Rosetta mission: Flying towards the origin of the solar system. *Space Science Reviews*, 128(1–4), 1–21.
- Hand, E. (2014). Philae probe makes bumpy touchdown on a comet. *Science*, 346(6212), 900–901.
- Hockman, B., Frick, A., Nesnas, I. A. D., & Pavone, M. (2015). Design, control, and experimentation of internally-actuated rovers for the exploration of low-gravity planetary bodies. In *Conference on Field and Service Robotics*, Toronto. In press.
- JAXA Hayabusa mission. (2011). Technical report, JAXA. Available at <http://hayabusa.jaxa.jp/e/index.html>.
- Jones, R. (2000). The MUSES-CN rover and asteroid exploration mission. In *22nd International Symposium on Space Technology and Science* (pp. 2403–2410).
- JPL's Cubesats. (2015). Technical report, JAXA. Available at <http://cubesat.jpl.nasa.gov/>.
- Klingelhöfer, G., Brückner, J., Duston, C., Gellert, R., & Rieder, R. (2007). The Rosetta alpha particle X-ray spectrometer (APXS). *Space Science Reviews*, 128(1–4), 383–396.
- McGeer, T. (1990). Passive dynamic walking. *International Journal of Robotics Research*, 9(2), 62–82.
- McNutt, L., Johnson, L., Clardy, D., Castillo Rogez, J., Frick, A., & Jones, L. (2014). Near-Earth asteroid scout. In *AIAA Space 2014 Conference*, San Diego.
- NASA space technology roadmaps and priorities: Restoring NASA's technological edge and paving the way for a new era in space. (2012). Technical report, National Research Council.
- Nicewarner, K., & Dorais, G. (2006). Designing and validating an adjustably-autonomous free-flying intraspacecraft robot. In *Space* (p. 7395).
- Pilorget, C., Bibring, J.-P., & Berthe, M. (2011). MicrOmega: An IR hyperspectral microscope for the Phobos Grunt Lander. In *Lunar and Planetary Science Conference* (vol. 42, p. 1930).
- Reid, R. G., Roveda, L., Nesnas, I. A. D., & Pavone, M. (2014). Contact dynamics of internally-actuated platforms for the exploration of small solar system bodies. In *i-SAIRAS* (pp. 1–9), Montréal, Canada.
- Romanishin, J. W., Gilpin, K., & Rus, D. (2013). M-blocks: Momentum-driven, magnetic modular robots. In *IEEE/RSJ International Conference on Intelligent Robots and Systems* (pp. 4288–4295). IEEE.
- Sagdeev, R. Z., & Zakharov, A. V. (1989). Brief history of the Phobos mission. *Nature*, 341(6243), 581–585.
- Valle, P., Dungan, L., Cunningham, T., Lieberman, A., & Poncia, D. (2011). Active response gravity offload system. Available at <http://www.techbriefs.com/component/content/article/ntb/tech-briefs/mechanics-and-machinery/10855>.
- Wilcox, B. H. (2012). ATHLETE: A limbed vehicle for solar system exploration. In *IEEE Aerospace Conference* (pp. 1–9). IEEE.
- Yoshimitsu, T., Kubota, T., Nakatani, I., Adachi, T., & Saito, H. (1999). Microgravity experiment of hopping rover. In *Proceedings of the IEEE Conference on Robotics and Automation* (vol. 4, pp. 2692–2697).